

Reaching a burning plasma and ignition using smaller capsules/*Hohlraums*, higher radiation temperatures, and thicker ablators/ice on the national ignition facility

Cite as: Phys. Plasmas **30**, 032702 (2023); <https://doi.org/10.1063/5.0131180>

Submitted: 18 October 2022 • Accepted: 25 January 2023 • Published Online: 06 March 2023

 K. L. Baker, C. A. Thomas,  O. L. Landen, et al.



View Online



Export Citation



CrossMark



Physics of Plasmas
Features in Plasma Physics Webinars
Register Today!

 AIP Publishing

Reaching a burning plasma and ignition using smaller capsules/*Hohlraums*, higher radiation temperatures, and thicker ablator/ice on the national ignition facility

Cite as: Phys. Plasmas **30**, 032702 (2023); doi: 10.1063/5.0131180

Submitted: 18 October 2022 · Accepted: 25 January 2023 ·

Published Online: 6 March 2023



View Online



Export Citation



CrossMark

K. L. Baker,^{1,a)} C. A. Thomas,² O. L. Landen,¹ S. Haan,¹ J. D. Lindl,¹ D. T. Casey,¹ C. Young,¹ R. Nora,¹ O. A. Hurricane,¹ D. A. Callahan,¹ O. Jones,¹ L. Berzak Hopkins,¹ S. Khan,¹ B. K. Spears,¹ S. Le Pape,¹ N. B. Meezan,¹ D. D. Ho,¹ T. Döppner,¹ D. Hinkel,¹ E. L. Dewald,¹ R. Tommasini,¹ M. Hohenberger,¹ C. Weber,¹ D. Clark,¹ D. T. Woods,¹ J. L. Milovich,¹ D. Strozzi,¹ A. Kritchler,¹ H. F. Robey,³ J. S. Ross,¹ V. A. Smalyuk,¹ P. A. Amendt,¹ B. Bachmann,¹ L. R. Benedetti,¹ R. Bionta,¹ P. M. Celliers,¹ D. Fittinghoff,¹ C. Goyon,¹ R. Hatarik,¹ N. Izumi,¹ M. Gatu Johnson,⁴ G. Kyrala,³ T. Ma,¹ K. Meaney,³ M. Millot,¹ S. R. Nagel,¹ P. K. Patel,¹ D. Turnbull,² P. L. Volegov,³ C. Yeamans,¹ and C. Wilde³

AFFILIATIONS

¹Lawrence Livermore National Laboratory, Livermore, California 94550, USA

²Laboratory for Laser Energetics, University of Rochester, Rochester, New York 14623, USA

³Los Alamos National Laboratory, Los Alamos, New Mexico 87544, USA

⁴Massachusetts Institute of Technology, Cambridge, Massachusetts 02139, USA

^{a)}Author to whom correspondence should be addressed: baker7@llnl.gov

ABSTRACT

In indirect-drive implosions, the final core hot spot energy and pressure and, hence, neutron yield attainable in 1D increase with increasing laser peak power and, hence, radiation drive temperature at the fixed capsule and *Hohlraum* size. We present simple analytic scalings validated by 1D simulations that quantify the improvement in performance and use this to explain existing data and simulation trends. Extrapolating to the 500 TW National Ignition Facility peak power limit in a low gas-fill 5.4 mm diameter *Hohlraum* based on existing high adiabat implosion data at 400 TW, 1.3 MJ and 1×10^{16} yield, we find that a $2\text{--}3 \times 10^{17}$ yield (0.5–0.7 MJ) is plausible using only 1.8 MJ of laser energy. Based on existing data varying deuterium–tritium (DT) fuel thickness and dopant areal density, further improvements should be possible by increasing DT fuel areal density, and hence confinement time and yield amplification.

Published under an exclusive license by AIP Publishing. <https://doi.org/10.1063/5.0131180>

I. INTRODUCTION

In indirect drive inertial confinement fusion (ICF) at National Ignition Facility (NIF), a deuterium–tritium (DT) filled capsule^{1,2} is driven by x-rays at peak radiation temperatures T_r of ~ 300 eV produced by irradiating the inside of a high-Z *Hohlraum* with 192 laser beams entering through two laser entrance holes (LEHs) on either end. The DT hotspot must reach high ion temperatures, $T_{ion} > 5$ keV, and high areal densities, $\rho r > 0.2\text{--}0.3$ g/cm², to initiate burn, while the total yield depends on the confinement time provided by the total areal density of the DT and remaining ablator, typically designed at 1–2 g/cm².

The goal of the National Ignition Facility (NIF) is to increase the liberated fusion energy “yield” in inertial confinement fusion (ICF) experiments well past the ignition threshold and the input laser energy. Most recent efforts have focused on increasing the capsule size to increase the capsule-absorbed energy. By using smaller *Hohlraums* with less wall losses, which was the approach pursued in Refs. 3 and 4 the peak radiation drive temperature T_r can be increased, such that the capsule-absorbed energy for smaller capsules can be comparable to larger capsules placed in bigger *Hohlraums*. In addition, the higher T_r leads to higher ablation and, hence, stagnation pressures for equivalent peak implosion velocity.⁵ In this paper, we present the results of two sets of DT-layered implosions, both of which used 0.844 mm inner

radius high-density carbon (HDC) ablators in small *Hohlraums*. The BigFoot experimental campaign^{3,4,6–15} is shown to follow analytic scaling with laser power and when plotted as a function of capsule-absorbed energy to account for differences in the *Hohlraum* configurations, both the BigFoot and high-density carbon (HDC)^{16–21} campaigns are shown to follow the same scaling with yield amplification vs capsule-absorbed energy. Extrapolating the experimental performance of these two campaigns and interpolating the simulations, which match the experiment observables at lower energies, indicate that these implosions would cross into the burning plasma regime at ~ 1.5 MJ of laser energy. These simulations also predict, assuming low laser plasma backscatter losses and symmetry control can be maintained, that these implosions could reach ignition with a capsule-absorbed energy ~ 175 kJ, ~ 1.8 MJ of laser energy into a gold-lined *Hohlraum* with 3.45 mm LEHs, with appropriate thicker fuel and ablator.^{3,4} With the typical NIF laser energy of 1.85 MJ and Au-lined DU *Hohlraums* with 3.1 mm LEHs, this platform could drive these capsules with up to 200 kJ of capsule-absorbed energy and *Hohlraum* temperatures of >335 eV. To help support this, we also present experimental results in which we were able to increase the stagnated cold fuel areal density, by increasing the initial ice thickness. The ability to increase the remaining ablator and cold fuel areal density is critical in increasing confinement time and, hence, achieving a larger burn-up fraction of the assembled DT fuel and, hence, higher neutron yield.

In Sec. II, we briefly review the benefits of using smaller capsules and *Hohlraums* using the *Hohlraum* power balance formula. In Sec. III, we review the experimental parameters from the high-density carbon-based ablator campaign, denoted BigFoot, performed in the smallest 5.4 mm radius *Hohlraums* which used the 192 beam NIF. In Sec. IV, we present simplified capsule rocket model scalings for the purpose of extrapolating from existing data and validate them by comparing to simulation outputs of implosion velocity and mass remaining trends with increasing peak power, laser energy, and initial capsule mass. In Sec. V, we present analytic scalings of hot spot energy, pressure, and ignition metrics in the absence of alpha heating, validated to 1D simulation results and compare to data and Bigfoot design trends. In Sec. VI, we use the analytic formalism to extrapolate to NIF peak power at fixed *Hohlraum* and capsule size, including a discussion of other potential issues such as symmetry control and losses due to laser-plasma instabilities. In Sec. VII, we include yield amplification by alpha heating, first comparing the BigFoot data with many of the campaigns that were carried out on the NIF at higher power and energies in larger *Hohlraums* driving larger capsules, then extrapolating to NIF peak power using a simulated correspondence between the generalized Lawson criterion and yield amplification. In Sec. VIII, we discuss the benefits of increasing the DT fuel layer and present the empirical scaling of inferred stagnated fuel areal density as a function of the initial ice thickness. In Sec. IX, we summarize the results and extrapolations of the BigFoot 844 design with 0.844 mm I.R. HDC capsules and potential further improvements.

II. HOHLRAUM POWER BALANCE

The peak temperature in a *Hohlraum* can be approximated as a power balance between the x-ray power produced in the *Hohlraum* given by the product of peak laser power P_L and fraction converted to x-rays β , and the x-ray power lost to the walls of the *Hohlraum*, the capsule itself, and the laser entrance holes (LEH).^{6,22,23} We note that β

also accounts for the fraction of laser peak power lost to backscatter and the *Hohlraum* He gas-fill used to tamp the high Z *Hohlraum* walls, a few % for the low He gas-fills used currently. The power lost to the walls, capsule, and out the LEHs is the x-ray flux inside the *Hohlraum*, σT_r^4 , multiplied by their respective surface areas at peak power and the fraction $(1 - \alpha)$ not reradiated, where α is an albedo, yielding:

$$\beta P_L = \sigma T_r^4 [A_w(1 - \alpha_w) + 4\pi R_c^2(1 - \alpha_c) + 2\pi R_{LEH}^2], \quad (1)$$

where we can define an effective loss area $[A_w(1 - \alpha_w) + 4\pi R_c^2(1 - \alpha_c) + 2\pi R_{LEH}^2]$. Typically, $\beta \approx 0.75$ and the ratio of the three terms in the effective loss area comprise 60%, 10%, and 30% of the total losses²² with $\alpha_c \approx 0.3$ and $\alpha_w \approx 0.85$ averaged over peak power for the highest practical atomic number Au or U walls available. As T_r increases, by either increasing peak laser power or reducing losses, the albedos also increase such that $T_r^{3.5} \sim P_L$, a scaling used later. The effective loss area of the *Hohlraum* can be minimized by reducing the *Hohlraum* wall's area, increasing the *Hohlraum* wall's albedo, reducing the size of the capsule or reducing the size of the LEH. Most layered implosions use a gold-lined uranium wall to maximize the *Hohlraum* wall's albedo. The minimum LEH size on the NIF is currently limited by the phase plates used by the inner beams. The LEH diameter must be larger than $\sim 1.2 \times$ the inner beam footprint in the LEH plane. The two remaining techniques to reduce the losses in the *Hohlraum* are reducing the surface area of the *Hohlraum* wall and the capsule, the strategy employed here.

III. EXPERIMENTAL DESIGN

This paper primarily extrapolates from the NIF campaign, denoted as the BigFoot 844, which used partially W-doped high-density carbon (HDC) ablators of inside radius 0.844 mm and thickness between 64 and 68 μm and deuterium-tritium fuel layers between 41 and 45 μm thick. This BigFoot 844 campaign^{3,4,6} was conducted in 5.4 mm diameter by 10.13 mm length *Hohlraums* filled with 0.3 mg/cm^3 helium gas and equipped with 3.45 mm LEHs covered with $0.5 \mu\text{m}$ Lexan windows. The 44.5° and 50° cones were separated in z where they impact the *Hohlraum* wall and each of the outer quads was separated into groups of two beams containing orthogonal polarizations displaced in azimuth to create more uniform illumination of the *Hohlraum* wall. Cone and quad splitting the outers also reduced the intensity on the wall which reduced the gold bubble expansion velocity where the outer laser beams hit the *Hohlraum* wall to maintain symmetry control and decrease the growth of laser-plasma instabilities. The BigFoot 844 campaign was designed such that the second shock overtook the first shock in the ablator near the ablator-ice interface with the third overtaking the first two in the gas near the gas-ice interface. As such the ablator was shocked three times and the ice was only shocked twice. This had the effect of stabilizing the fuel-ablator interface, driving a stable (negative) fuel-ablator Atwood number, A, in the acceleration phase of the implosion, where $A = (\rho_f - \rho_a)/(\rho_f + \rho_a)$ (Ref. 3). Thus, the density of the ablator, ρ_a , is greater than the density of the fuel, ρ_f , throughout acceleration. This was, however, at the expense of a high-design fuel adiabat, ~ 4 , due to the larger first combined shock velocity entering the ice layer. The BigFoot design also had the advantage that it required a shorter foot which reduced the ablated mass under inefficient low T_b , low exhaust velocity $\sim \sqrt{T_r}$ conditions. Combined with the use of a 20%–30% thinner fuel layer,

this leaves more ablator mass remaining for a given peak implosion velocity, as discussed and tabulated further in Sec. IV. The main campaign included four layered DT shots progressively increasing peak power from 310 to 400 TW, laser energy from 1.05 to 1.35 MJ, initial ablator thickness from 64 to 68 μm , and DT fuel thickness from 41 to 45 μm .

IV. SIMULATED AND ANALYTIC IMPLOSION SENSITIVITIES

The approach proposed in this article and Refs. 3 and 4 is to increase the velocity and performance of a set of BigFoot implosions sharing a fixed capsule design by increasing the laser peak power and energy until a performance cliff is reached due to insufficient ablator mass remaining and too much hydro growth. Just before that point, the capsule and DT ice thickness would be increased to maintain the implosion velocity as laser energy E_L is increased. To anchor this strategy, a series of simulations performed^{3,4} using the two-dimensional radiation hydrodynamics code Lasnex^{24,25} were presented for the Bigfoot 844 campaign, 0.844 mm radius capsule implosions, starting from the two 320 and 330 TW existing implosions at the time and extending to 500 TW. The two lowest energy simulations were post-shots of N161030 and N170109, and the remaining four represent a systematic walkup to the full NIF power. Subsequent experiments at 400 TW, N190721 and N190617, agreed within the error bars, with the simulation and occurred after the BF 950 platform had begun. The simulations used the technique of adding preheat energy, 0.75 MJ/g, to the DT ice layer a few hundred picoseconds before the time of peak

implosion velocity (over a period of 100 ps) which increased the design adiabat from $\alpha \sim 4$ to $\alpha \sim 5.5$. Adding preheat energy to the DT ice layer allowed the postshot simulations to more accurately reproduce the experimentally measured yield, down-scattered ratio (DSR), T_{ion} and hotspot size and is a surrogate for mix and shock mistiming.

Simulation inputs and outputs are shown in Fig. 1 and Table I. For all but the 500 TW simulation, the capsule mass and laser peak power pulse length τ are kept fixed as peak power increases. Figure 1(b) shows the corresponding remaining mass and coast time decreases as expected as laser power (P_L), energy ($E_L \sim P_L \tau$), and T_r are increased. The coast time is defined as the time between when the laser pulse has dropped to half of its peak power and the time of peak gamma-ray emission, bang time. We note the coast time is kept below 1 ns, a typical *Hohlraum* flux cooling time, as data and simulations show this to be crucial to maintaining high ablation pressure at peak velocity. The simulation performed at 500 TW, 1.9 MJ increased the DT fuel and ablator thickness 20% to prevent burnthrough and mitigate the effects of hydrodynamic instability growth. This leads to the increase in mass remaining and leveling off of the peak fuel implosion velocity in Fig. 1(c).

For quantitatively understanding the simulation trends and extrapolating from newer data, it is instructive to evaluate more broadly the scalings of peak implosion velocity and mass remaining with capsule mass and peak radiation T_r using a simplified analytic treatment. In the spherical rocket model of an indirect-drive ICF implosion, the peak implosion velocity, v_{imp} , can be expressed in terms of the peak power radiation temperature, T_r ; the initial combined mass of the ablator and DT ice, M ; and the remaining combined

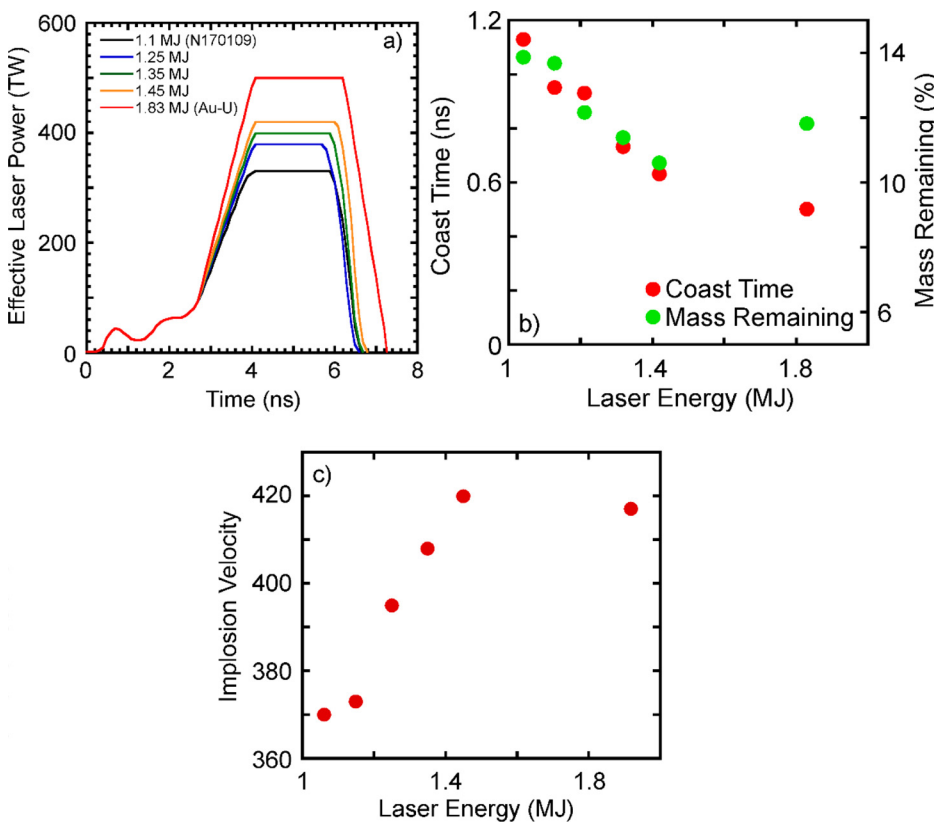


FIG. 1. (a) Pulse shapes, (b) ablator remaining mass and coast times, and (c) peak fuel implosion velocity for the simulations performed for Ref. 1.

TABLE I. Simulated hotspot variables used to calculate the hotspot pressure and yield amplifications for BigFoot 844 designs as increase laser peak power and energy.

Sim. Results	Laser energy (MJ)	Laser power (TW)	Ablator thickness (μm)	DT fuel thickness (μm)	Peak implosion velocity ($\mu\text{m/ns}$)	Ablator mass rem. (%)	Coast time (ns)	Primary yield	Ion temp. (keV)	DSR (%)	Hotspot pressure (Gbar)	Y_{amp}
N161030	1.06	318	63.8	40.4	370	9.8	1.13	2.1×10^{15}	3.91	2.68	180	1.6
N170109	1.15	332	63.8	41	372	9.6	1.07	3.7×10^{15}	4.06	2.79	244	1.8
X1	1.25	380	63.8	40	395	8.0	0.93	8.6×10^{15}	4.67	2.97	338	2.6
X2	1.35	400	63.8	40	409	7.3	0.73	1.2×10^{16}	5.03	3.02	395	3.1
X3	1.45	420	63.8	40	421	6.5	0.63	1.6×10^{16}	5.51	3.04	449	3.6
X4	1.9	500	76.6	48	417	8.4	0.5	9.6×10^{16}	7.56	3.5	775	21

ablator mass and DT ice mass, M_r ; as $v_{\text{imp}} \sim T_r^{0.5} \ln(M/M_r)$. Over the range of values of M/M_r in these implosions, $7 \leq M/M_r \leq 12$, $\ln(M/M_r)$ approximates as $0.73 \sqrt{(M/M_r)}$, hence,²⁶

$$v_{\text{imp}} \sim T_r^{0.5} \sqrt{(M/M_r)}. \quad (2)$$

The rocket equation approximation is valid between $2v_{\text{ex}} < v_{\text{imp}} < 2.5v_{\text{ex}}$, where the exhaust velocity v_{ex} is $\approx 10\sqrt{T_r}$ $\mu\text{m/ns}$, hence for v_{imp} between approximately 330 and 450 $\mu\text{m/ns}$ (Ref. 1). The mass ablation rate, dM/dt , for low Z ablators scales as $T_r^3 R^2$, where R is some fixed fraction of the initial radius R_c of the capsule.²⁷ The ablated capsule mass, $M - M_r \sim M$ since $M_r \ll M$, then scales over an implosion time τ as

$$dM/dt \sim M/\tau \sim T_r^3 R^2. \quad (3)$$

Case A: Constant Initial Ablator + Fuel Mass M :

Substituting for the implosion time $\tau \sim R/v_{\text{imp}}$ in Eq. (3) we arrive at,²⁸

$$v_{\text{imp}} \sim T_r^3 R^3 / M. \quad (4)$$

As expected, in the hydroscaling limit for which the peak T_r is kept constant and $R' = SR$, and $M' = S^3 M$ the implosion velocity is independent of scale S . Equation (4) represents the strong increase in v_{imp} as T_r is increased at fixed capsule R and M . Since $T_r^{3.5} \sim P_L$ for fixed *Hohraum* scale and pulse length, $v_{\text{imp}} \sim P_L^{6/7}$. With $v_{\text{imp}} \sim T_r^3 R^3 / M \sim R/\tau_{\text{acc}}$ and $P_L \sim T_r^{3.5}$, we can write the acceleration time, τ_{acc} , in terms of the laser power as $\tau_{\text{acc}} \sim P_L^{-6/7}$, where τ_{acc} is the time between the start of the peak laser power and ~ 400 ps before the bang time. This is consistent with the peak simulated fuel velocity increasing 13% between $P_L = 330$ and 420 TW on Fig. 1(c) and Table I, when accounting for peak shell v_{imp} relevant to the rocket model increasing faster than fuel velocity being squeezed inward, as ablator mass remaining drops per Fig. 1(b).²⁹

Case B: Constant Remaining Ablator + Fuel Mass M_r

We now consider the constraint of fixed minimum M_r that is desirable to keep soft x-rays from penetrating the shell and heating the DT fuel directly while still maximizing v_{imp} . Substituting for M from Eq. (2) in Eq. (4),

$$v_{\text{imp}} \sim T_r^{4/3} R M_r^{-1/3}. \quad (5)$$

Equation (5) approximates the more detailed derivation in Saillard Eq. (3.39), where $v_{\text{imp}} \sim T_r^{1.26} R M_r^{-1/3}$. The lower scaling with T_r can

be recovered by including a first-order correction in M_r/M . We note the drop in M_r as v_{imp} increases at fixed R and M , consistent with Fig. 1(b) simulations as increasing laser energy up to 1.45 MJ. With $v_{\text{imp}} \sim RT_r^{4/3} \sim R/\tau_{\text{acc}}$ and $P_L \sim T_r^{3.5}$, we can write the acceleration time, τ_{acc} , in terms of the laser power as $\tau_{\text{acc}} \sim P_L^{-0.38}$, where again τ_{acc} is the time between the start of the peak laser power and ~ 400 ps before the bang time. Substituting for v_{imp} in Eq. (2) using Eq. (5), the scaling of initial mass with peak T_r is given by

$$M \sim T_r^{5/3} R^2 M_r^{1/3}. \quad (6)$$

Equations (5) and (6) directly give the scaling of v_{imp} and M with increasing T_r for fixed R and M_r . We note that v_{imp} still increases faster than $v_{\text{ex}} \sim T_r^{0.5}$ as allowing for more ablation afforded by more laser energy and starting with higher capsule mass areal density M/R^2 . We can compare this to the rocket model for an indirect drive that yields¹ $v_{\text{imp}} \sim (R/\Delta R)v_{\text{abl}}$. The ablation rate v_{abl} is defined as $(dm/dt)/\rho \approx T_r^{0.9}$ since $dm/dt \sim T_r^3$, and for a given adiabat design, $\rho \sim P^{3/5} \sim T_r^{2.1}$. A more conservative limit,^{1,2} by keeping the in-flight capsule aspect ratio (IFAR = R/dR) fixed, therefore, yields $v_{\text{imp}} \sim T_r^{0.9}$.

Case C: Constant Peak Implosion Velocity, v_{imp}

For the even more conservative case, approximating that used in simulating the highest laser energy design point in Fig. 1, v_{imp} is held fixed as P_L is raised from 420 to 530 TW (530 Au-U) (E_L from 1.45 to 1.9 MJ) to raise T_r . That limit leads to Eq. (4) simplifying to

$$M \sim T_r^3 R^3. \quad (7)$$

As expected, M increases as a faster power of T_r than in Eq. (6), following the mass ablation rate scaling to the zeroth order. Rearranging Eqs. (5) and (2) at fixed v_{imp} , the scaling of mass remaining increases with T_r as

$$M_r \sim T_r^4 R^3, \quad (8)$$

and the fractional mass remaining M_r/M as

$$M_r/M \sim T_r. \quad (9)$$

Since $P_L \sim T_r^{3.5}$ from Sec. II, $M \sim P_L^{6/7}$ and $M_r/M \sim P_L^{2/7}$. Indeed, the design increases M by 20% as the laser power, P_L , is increased by $\approx 26\%$, from 420 to 530 TW (Au-lined DU). By contrast, the total fractional mass (ice + ablator) remaining M_r/M increases from 10.6% to 11.8%, an increase of $\sim 11\%$, vs the 7% predicted analytically.

For mitigating hydro-instability feedthrough from the ablation front and maximizing confinement time, the remaining ablator areal

density $\sim M_r/R_{hs}^2$ should be maximized. For a given design implosion adiabat and v_{imp} , the convergence ratio $\sim R/R_{hs}$ of the implosion is conserved, hence, Eq. (7) can be rearranged to give

$$M_r/R_{hs}^2 \sim T_r^4 R \sim (P_L/R_H^2)^{8/7} R \approx P_L(R/R_H)/R_H, \quad (10)$$

where R_H is the *Hohlraum* radius. The key point of Eq. (10) is that for the optimum strategy of operating at maximum P_L and R/R_H to optimize coupled energy and still allow for sufficiently uniform x-ray illumination at the capsule, the remaining shell areal density scales as $1/R_H$. For the conservative limit of keeping the in-flight-aspect-ratio (IFAR) constant in case B, the implosion velocity can be expressed as $v_{imp} \propto (R/\Delta R)(T_r)^{0.9}$ (Ref. 1). Thus, for a fixed implosion velocity, the IFAR is approximately inversely related to the *Hohlraum* radiation temperature, T_r . Likewise, the total number of e-foldings of amplification of perturbations of mode m due to the combined effects of acceleration and feedthrough can be expressed in terms of the IFAR as $\sim \text{sqrt}(m/(1 + 0.2m/\text{IFAR})) - 1.8m/\text{IFAR}$.¹ For a 6% increase in T_r , one would expect an $\sim 6\%$ decrease in IFAR and a corresponding reduction in the growth factors for a particular mode number. This increase in implosion robustness at a smaller scale, all else equal, represents an additional advantage to higher T_r increasing the ablation pressure at a given implosion speed,²⁸ lower in-flight-aspect-ratio defined as outer ablator radius divided by the total shell thickness, and stronger ablative stabilization.²²

V. HOTSPOT METRICS WITHOUT ALPHA HEATING

The simulated product $E_{hs}P_{hs}^2$ for implosions is a convenient metric³⁰ for the likelihood of ignition, where E_{hs} and P_{hs} are the hotspot energy and pressure at minimum volume in the absence of alpha-heating. We now consider the scaling of hot spot energy E_{hs} and pressure P_{hs} with peak power P_L under the constraints of fixed adiabat and capsule and *Hohlraum* scale. We will start by assuming case C that the implosion time $\sim R/v_{imp}$ and, hence, the peak implosion velocity v_{imp} is approximately held fixed as P_L , and hence, T_r is increased by appropriately thickening up the capsule and DT fuel. That will ensure nearly fixed *Hohlraum* to capsule coupling efficiency. Moreover, simulations of ignition-relevant indirect-drive designs show that the coupling efficiency to the capsule kinetic energy at peak v_{imp} , known as “rocket efficiency,” is a weak function of any mass remaining² and v_{imp} variability. Finally, the coupling efficiency η_{hs} of imploding kinetic energy $1/2M_r v_{imp}^2$ to E_{hs} in indirect-drive, for fixed v_{imp} and the ratio of DT fuel mass M_{DT} to total remaining mass M_r , is \approx constant, at $\approx 25\%$ near ignition of HDC-based designs.³⁰ Hence, simulations under this constraint of fixed *Hohlraum* and capsule scale and v_{imp} , and increasing M_{DT} in proportion to M_r as approximately designed between 420 and 530 (Au-lined DU) TW per Fig. 1 and Table I, predict E_{hs} approximately scaling with P_L . We can understand this by applying the simplified rocket model developed in Sec. IV. Substituting for v_{imp} from Eq. (2),

$$E_{hs} \sim \eta M_r V_{imp}^2 \sim T_r M \quad (11)$$

and further substituting for M using Eq. (7),

$$E_{hs} \sim T_r^4 R^3 \sim P_L^{8/7}. \quad (12)$$

We now wish to evaluate P_{hs} . We start with assuming adiabatic hot spot compression (PV^γ conserved) between the time of peak

velocity (subscript pv) and stagnation (subscript hs)^{9,31} such that assuming ideal gas $\gamma = 5/3$,

$$P_{hs} R_{hs}^5 \sim P_{pv} R_{pv}^5. \quad (13)$$

Equation (13) has implicitly assumed the pdV work dominates over the sum of the alpha heating gains and radiative losses.³² That sum is 0 at $T_{ion} \sim 4.3$ keV, typical of the lowest yield implosions considered here that are used to normalize the scaling. 1D simulations³⁰ show that R_{pv} is constant to the 1% level as peak T_r is varied for a given low coast implosion design, so we can simplify to

$$P_{hs} R_{hs}^5 \sim P_{pv} \sim T_r^{3.5} \sim P_L, \quad (14)$$

where we have equated pressure at peak v_{imp} as scaling with peak ablation pressure $\sim T_r^{3.5}$, which is valid for short coast times, < 0.5 ns.³³ Substituting for R_{hs} from Eq. (14) into the definition of $P_{hs} \sim E_{hs}/R_{hs}^3$ and for E_{hs} using Eq. (12),

$$P_{hs} \sim T_r^{19/4} \sim P_L^{9.5/7}. \quad (15)$$

Hence, the ignition metric $E_{hs}P_{hs}^2$ scales as $P_L^{27/7}$ for fixed v_{imp} (case C), increasing by a significant $2.0\times$ between the $P_L = 420$ and 500 TW designs.

Figures 2(a) and 2(b) show the measured (green circles) and simulated (black circles) hotspot pressures [Fig. 2(a)] and energies [Fig. 2(b)] for the BigFoot 844 campaign. These were calculated assuming a uniform hotspot model and included alpha heating.³⁴ To understand the contribution to alpha heating, a dataset of implosions with a wide range of final adiabats, with and without alpha heating, was used to determine the pressure (P_{hs_amp}) and energy (E_{hs_amp}) amplification factor as a function of yield amplification.³⁵ For this database, the pressures and energies were again calculated using the uniform hotspot model, and the fits to the pressure and energy amplifications are listed in Figs. 2(a) and 2(b), respectively. The with-alpha heating curves in the figures are then the without-alpha analytic results multiplied by the amplification factors. The circle diameters of the with-alpha heating numbers are proportional to the square root of the yield amplification.

For case A, assuming fixed M , we start with Eq. (2) including η_{hs} ,

$$E_{hs} \sim \eta_{hs} M_r V_{imp}^2 \sim \eta_{hs} T_r M \sim P_L^{11/7}, \quad (16)$$

where the last expression is derived from 1D simulations³⁰ showing that η_{hs} scales as $P_L^{9/7}$ for fixed M . We can understand this by recognizing that η_{hs} is the ratio³⁰ of hotspot volume R_{hs}^3 to total shell + hot spot volume $(R_{hs} + \Delta R)^3$ assuming an isobaric system. The shell thickness ΔR decreases as increase P_L , both due to increased P_{pv} and, hence, stagnated shell density and due to a larger fraction of the remaining mass being the cooler, hence denser DT fuel. Hence using Eqs. (14) and (16), $P_{hs} \sim P_L^{17/7}$ and the ignition metric $E_{hs}P_{hs}^2$ scales as $P_L^{45/7}$ for fixed M . We also note that $R_{hs} \sim (E_{hs}/P_{hs})^{1/3} \sim P_L^{-2/7} \sim 1/T_r$, shrinking slightly as laser power and ablation pressure increase in the absence of alpha heating, consistent with those same simulations. Again, the with-alpha heating curves in Figs. 2(a) and 2(b) are the without-alpha analytic results multiplied by the amplification factors. Thus, in 1D, E_{hs} , P_{hs} and the ignition metric scale faster with P_L as we transition from the most conservative case C, fixed v_{imp} , to the least conservative case A, fixed M . Based on the good match between data, simulated, and analytic power laws, we estimate that the

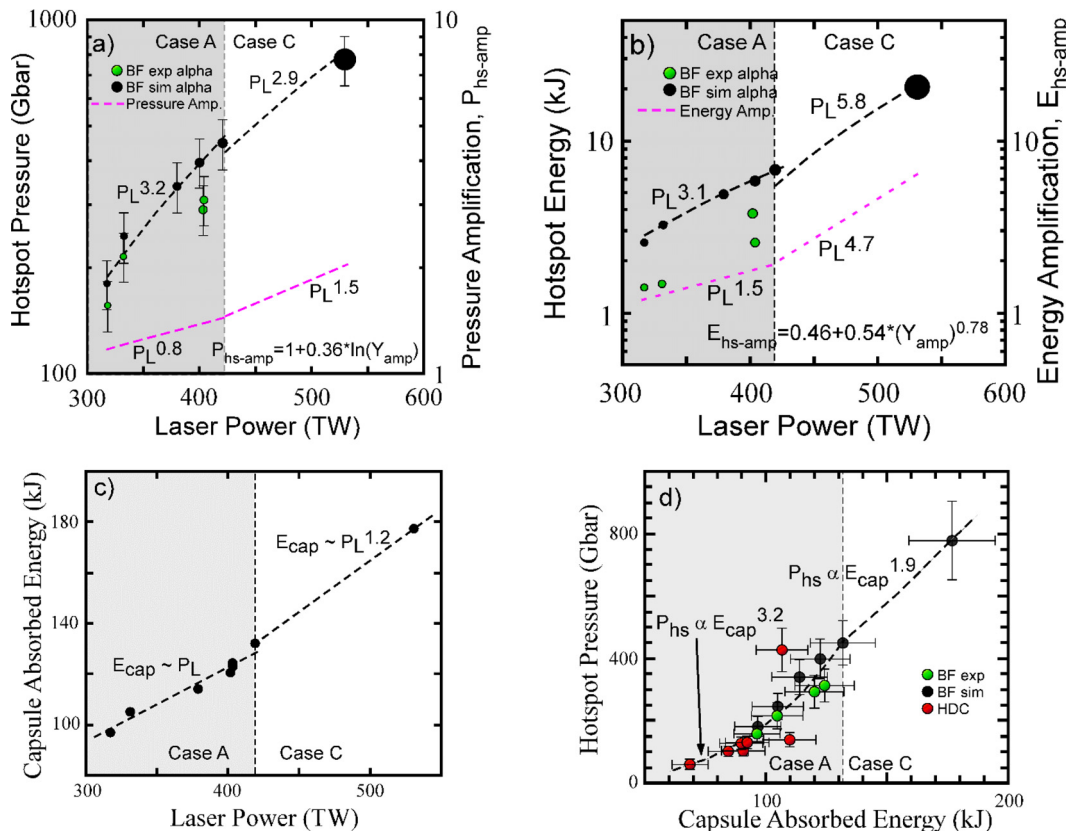


FIG. 2. (a) Hot spot pressure vs peak power for BigFoot data (green points) and simulations (black points). Overplotted curve is analytic scaling valid for pressures below 400 Gbar. (b) Hot spot energy vs peak power for BigFoot data (green points) and simulations (black points) overplotted with analytic scaling. (c) Capsule-absorbed energy vs peak power for BigFoot data (green points) and simulations (black points) overplotted with analytic scaling. (d) Hot spot pressure vs capsule-absorbed energy for BigFoot data (green points) and simulations (black points) and HDC data (red points) overplotted with analytic scaling.

power law exponents in the analytic model are good to 10%–20% over the ranges displayed.

Case B, assuming fixed M_r , applies closest to the transition between the 325 and 500 TW BigFoot shots. Substituting for v_{imp} from Eq. (5) and assuming an intermediate scaling $\eta_{hs} \sim P_L^{0.5}$,

$$E_{hs} \sim \eta_{hs} M_r v_{imp}^2 \sim \eta_{hs} T_r^{8/3} R^2 M_r^{1/3} \sim \eta_{hs} P_L^{16/21} \sim P_L^{53/42}, \quad (17)$$

and using Eqs. (14), (17), and (5),

$$P_{hs} \sim P_L^{139/84} \sim T_r^{139/24} \sim v_{imp}^{139/32}. \quad (18)$$

As a check, we note the final expression matches the detailed derivation for case B in Ref. 36 [Eq. (4.45)] $P_{hs} \sim v_{imp}^{14/3}$. The ignition metric $E_{hs} P_{hs}^2$ then scales as $P_L^{32/7}$ for fixed M_r .

We can compare campaigns using different *Hohlraum* configurations by plotting capsule-absorbed energy. The capsule-absorbed energy can be approximated as $E_{cap} = 57(R_c)^2 E_L L_m / A_L$, where R_c is the capsule outer radius in mm, L_m is the *Hohlraum* wall material multiplier (1 for Au, 1.06 for U, or 1.065 for Au-lined U), A_L is the *Hohlraum* loss area in cm^2 calculated from Eq. (1) (assuming a wall albedo of 0.86), and E_L is laser energy delivered to the *Hohlraum*

(reduced by the inferred level of backscatter). This simple expression for the capsule-absorbed energy agrees fairly well with a sampling of the capsule-absorbed energy derived from integrated *Hohlraum* and capsule-only simulations. We obtain similar results using the definition $E_{cap} = 100(R_i)^3 P_L L_m / (A_L v_{imp})$, where E_L is replaced by $P_L R_i / v_{imp}$. In this case, P_L is the peak laser power delivered to the *Hohlraum* (reduced by the inferred level of backscatter), R_i is the capsule inner radius in mm, and v_{imp} is the peak implosion velocity. In Fig. 2(c), we have plotted the capsule-absorbed energy as a function of laser power for the BigFoot 844 implosion simulations. In Fig. 2(d), we use the results from Fig. 2(c) to show the pressure vs capsule-absorbed energy where we have now included the HDC 844 campaign which also used 0.844 mm inner radius capsules. By plotting the pressure in terms of capsule-absorbed energy, we can see that the different campaigns have a similar pressure vs capsule-absorbed energy curve even though the experiments were carried out in different size *Hohlraums* with different laser energies and powers. We note that the capsule-absorbed energies (E_{cap}) for the BigFoot and HDC 844 implosions are all less than 130 kJ at the modest laser energies and wall materials of the experiments were carried out in but that they could be pushed to 200 kJ.

TABLE II. Input and output parameters for 400 TW N190721 and analytic extrapolations to 500 TW under various constraints.

Shot or design	Eff laser power (TW)	Peak power duration (ns)	Laser energy (MJ)	Peak T_r (eV)	Ablator thickness (μm)	DT Fuel thickness (μm)	v_{imp} ($\mu\text{m/ns}$)	M_r/M (%)	EP^2 (norm)
N190721	400	2.1	1.3	300	68	45	400	12	1
Fixed M_r	500	1.75	1.35	320	68	45	480	8	4.2
Fixed M_r	500	1.9	1.5	320	76	45	437	10.7	2.8
Fixed v_{imp}	500	2.1	1.6	320	82	45	400	12.8	2.4
Fixed M_r DU	530	1.9	1.6	325	78	45	446	10.4	3.6

VI. PEAK POWER EXTRAPOLATION

We now have all the formulas required for scaling hot spot performance from the existing shot N190721 at 400 TW (Au *Hohlraum*) to the current NIF peak power capability of 500 TW (effectively 530 TW in an Au-lined U *Hohlraum*). The foot pulse length will be assumed to scale with ablator + DT fuel thickness, hence, approximately as M for fixed R . The peak power duration τ should scale as $1/v_{\text{imp}}$ for assuring constant coast time, hence, E_L scales \approx as P_L/v_{imp} by ignoring any foot length and, hence, foot energy changes at $10\times$ lower power mandated by capsule thickness changes. **Table II** gives the various input and output values for extrapolating from N190721 400 to 500 TW peak power assuming the three cases of constant M , constant M_r , and constant v_{imp} . In addition, we have added a case for constant M_r replacing the Au with Au-lined DU *Hohlraum* that is predicted based on prior data^{37–39} to increase wall albedo such that the effective peak power is 6% larger per Eq. (1). Also listed on the last column of **Table II** is the ignition metric $E_{\text{hs}}P_{\text{hs}}^2$ normalized to N190721. The threat of x-rays burning through the ablator and leading to unstable Atwood number at ablator/fuel interface or penetration of ablation front hydrodynamic instability growth suggests keeping $M_r/M > 9\%$ such that the remaining ablator mass is no less than the 4%–4.5%, equivalent to the DT fuel mass. Combined with maximizing the ignition metric, we choose to concentrate on further exploring the fixed

M_r case ultimately using an Au-lined U *Hohlraum* for higher coupling efficiency. This suggests that the ignition metric can be increased $3.6\times$.

Figure 3 compares the pulse shape used for N190721 to the pulse shape required for maintaining fixed M_r at the maximum NIF peak power of 500 TW per the analytic scalings presented earlier. The pulse foot is 12% longer to provide the same shock timing for the 12% higher mass capsule, while the peak power duration $\tau \sim 1/v_{\text{imp}}$ is 9% shorter. A rocket model of the two pulse shapes/designs predicts that their percentage mass remaining is within 10% of one another, 7.3% vs 7.8%.

It is worthwhile revisiting at this point increasing the scale since **Table II** shows the full NIF 1.9 MJ energy not being used given the short (<3 ns) implosion times. Per Eq. (1), in the BigFoot 844 platform, with a 0.844 mm I.R. capsule in a 5.4×10.13 mm gold *Hohlraum* with 3.45 mm LEHs, the surface wall area of the *Hohlraum* is 1.86 cm^2 with an effective loss area of 0.51 cm^2 . In comparison, the BigFoot 950 platform used a 0.95 mm I.R. capsule in a 6.0×11.3 mm gold *Hohlraum* with 3.9 mm LEHs. The wall area is 2.28 cm^2 which has an effective loss area of 0.64 cm^2 . Assuming that both *Hohlraums* are driven by the same 500 TW peak power pulse, then the peak power radiation flux inside the *Hohlraum*, T_r^4 , will be $0.64/0.51 = 1.25\times$ higher in the smaller *Hohlraum*. Per Eq. (12), the hot spot energy E_{hs} for the smaller *Hohlraum* and capsule is $1.25(0.844/0.95)^3 = 0.9\times$, smaller. However, since the smaller *Hohlraum* $P_{\text{hs}} \sim T_r^{19/4} = 1.3\times$ per Eq. (15) more by virtue of being hotter, its ignition metric $\sim E_{\text{hs}}P_{\text{hs}}^2$ is significantly higher, $1.5\times$.

We now consider the drive symmetry control and laser-plasma instability challenges at increased peak laser power. Going to full NIF power in the 5.4×10.13 mm *Hohlraums* with 0.844 mm inner radius HDC capsules is expected to have a small effect on implosion symmetry. Specifically, we expect based on empirical models^{40,41} of inner beam propagation impairment due to ballistic capsule ablation and outer beam spot wall blow-off that the longer foot would only produce a shift in the core x-ray emission P2 of $\sim 10.5 \mu\text{m}$. N190721 had a round neutron hotspot with an inner beam peak power cone fraction of 31%. Going to 500 TW on the NIF, we can increase the inner cone fraction to a maximum of 33% which reduces the asymmetry in P2 to $-4.5 \mu\text{m}$ which could be zeroed out with $< 0.5 \text{ \AA}$ of wavelength differential between the inner and outer cones promoting cross beam energy transfer (CBET). Time-dependent P2 symmetry swings can be mitigated using techniques such as staggering beam cones in time to counter wall motion.⁴²

Laser plasma instability losses could potentially limit the peak power absorbed, especially as the plasma filling density increases in the *Hohlraum* given 15% more incident laser energy and capsule ablation.

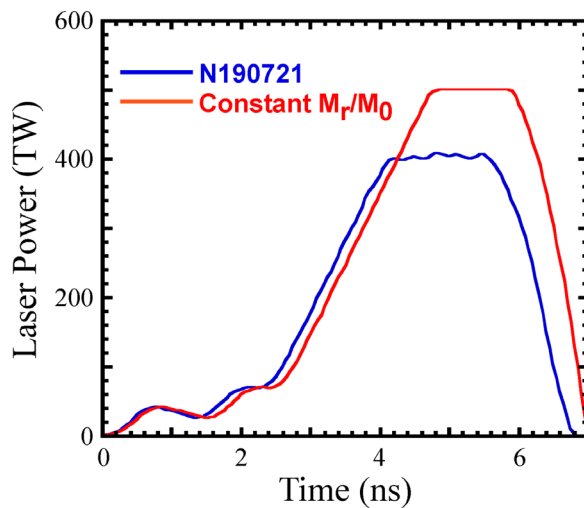


FIG. 3. Pulse shape for 400 TW N190721 and extrapolation to a 500 TW design to maintain \sim constant percentage mass remaining.

However, there are very few measured laser plasma instability (LPI) losses currently at 1.35 MJ, < 1%, and stimulated Brillouin scattering (SBS) on the 50° cone can be reduced by the application of a wavelength separation between 50° and 45° cones to promote CBET from the 50° to the 45° cone if it becomes a concern at higher power.⁴³ That leaves the potential of increased stimulated Raman scattering (SRS) losses on the inner beams due to both higher peak power and density, though to date no 0.3 mg/cm³ fill HDC campaign has measured any significant level of SRS. One could reduce the *Hohlraum* gas-fill slightly to counter the increased capsule ablation.

VII. YIELD AMPLIFICATION

In an inertially confined fusion (ICF) implosion with a DT fuel layer, each fusion reaction of deuterium and tritium ions generates a 14.1 MeV neutron and 3.5 MeV alpha-particle.⁷ The stopping ρR for an alpha-particle, however, is only $\sim 0.1\text{--}0.2 \text{ g/cm}^2$ at an ion temperature, T_{ion} , of 4 keV, which is characteristic of the hot-spot ρR and T_{ion} conditions achieved in many ICF implosions on the NIF. Each of the alpha particles stopped within the hot-spot deposited their 3.5 MeV of energy, thereby increasing the hotspot ion temperature, T_{ion} , and subsequently the reactivity rate. The alpha particles stopped in the cold fuel heat and ablate the fuel into the hot-spot, increasing the hotspot mass (M_{hs}) and the hot-spot ρR which enables more of the subsequent alpha particles to be stopped within the hot spot. When the fusion reactions heat the hotspot faster than loss mechanisms cool it, external energy is no longer required to heat the fuel and fusion ignition occurs. Another very important measure of performance in layered implosions is, therefore, the level of alpha heating present in the implosion.

The yield amplification, Y_{amp} , as a function of laser energy for the different NIF campaigns is shown in Fig. 4(a), where Y_{amp} is the

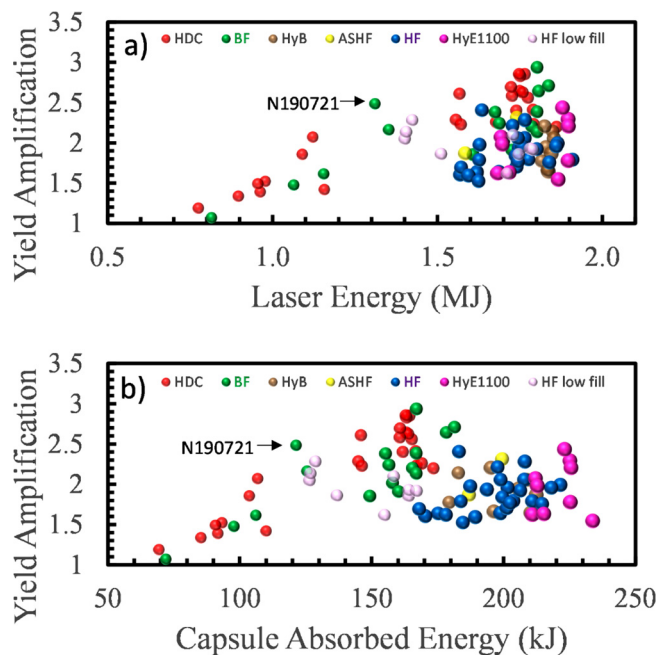


FIG. 4. Yield amplifications, Y_{amp} , as a function of (a) laser energy and (b) capsule-absorbed energy for numerous campaigns conducted on the NIF.

ratio of the measured yield in an experiment to the yield if there was no alpha heating or $Y_{\text{amp}} = Y_{\text{DT}}/Y_{\text{DT}\alpha\text{-off}}$. The yield amplification was calculated based on fitting simulations of BigFoot implosions using the formulas⁷

$$\text{ITFXmod} \sim (19.7 \times \text{DSR})^2 \times (0.24 \times (4f_{\text{DT}}) \times Y_{13-15}/M_{\text{fuel}}) \quad (19)$$

and

$$Y_{\text{amp-ITFXmod}} \sim \exp(\text{ITFXmod}^{0.446}), \quad (20)$$

where DSR is the down-scattered ratio (a ratio of the neutron yield in the fuel-scattered neutron kinetic energy range from 10–12 MeV to the 13–15 MeV unscattered yield), f_{D} is the deuterium fraction in the hotspot, f_{T} is the tritium fraction in the hotspot, Y_{13-15} is the primary neutron yield/ 10^{16} , and M_{fuel} is the initial mass of the ice layer in mg.

The diameter of the points in Fig. 4(a) represents symbolically the initial surface area of the capsule, ranging from an inner capsule radius of 0.833–1.1 mm. The Bigfoot shots are represented as green circles, whereas the shots performed with 0.844 mm capsules in the 5.4 × 10.13 mm *Hohlraums* are all below 1.4 MJ. The red circles are HDC shots below 1.2 MJ using three shocks all merging near the DT fuel/gas interface of 0.844 mm capsules in 5.75 × 10.13 mm *Hohlraums*. If we account for differing *Hohlraum* efficiency between gold (e.g., used for BigFoot), uranium (e.g., used for HDC), and gold-lined uranium-based campaigns, then, we can plot the yield amplification as a function of capsule-absorbed energy for the various campaigns in Fig. 4(b). We see that the capsule-absorbed energies (E_{cap}) for the BigFoot and HDC 844 implosions were less than 130 kJ at the laser energies and wall materials in which the experiments were carried out in. Hence, the 844 campaigns have been significantly more efficient at achieving a given yield amplification value approaching the burning plasma regime. In addition from Fig. 4(a), we can see that the BigFoot 844 implosion at 1.3 MJ and 400 TW, N190721, carried out in a gold *Hohlraum* achieved a higher yield amplification than the majority of the campaigns on the NIF conducted at full energy and power with higher albedo *Hohlraum* walls (including the HyE 1100,^{44,45} HyB,^{46,47} LF,^{38,48} HF,^{49–51} HF low fill,^{39,52} and ASHF^{53–55} campaigns). Only the BigFoot 950, HDC 910, Iraum 1000,⁵⁶ and HyE 1050^{57–59} campaigns achieved higher performance than N190721 but only achieved this at the full NIF energy and power. The question then becomes, what does it take for an 844 design to reach the burning plasma and ignition regime?

To assist in answering this, Fig. 5 highlights the four BigFoot 844 implosions, as smaller green circles, the BigFoot simulations,^{3,4} as black circles, the HDC 844 implosions, as red circles, as well as the neutron-imaged hot spot cores of the BigFoot experimental data. Also included are two Iraum, brown circles, and HyE 1050, gray circles, shots which recently crossed the burning plasma and the one HyE 1050 shot that crossed the ignition threshold.⁵⁹ As shown in Fig. 5(c), the simulated yield amplifications have ±20% error bars. This is consistent with measurements of Y_{amp} using deuterium-tritium/deuterium-tritium-hydrogen (DT/THD) pairs at lower yield amplification levels.⁷ The hotspot for N190617 at 1.35 MJ was very prolate, $P_2/P_0 \sim 56\%$, to which we attribute its drop in yield and yield amplification relative to a rounder hotspot. Interpolating the simulations, they predict that this BigFoot 844 platform would enter the burning plasma regime

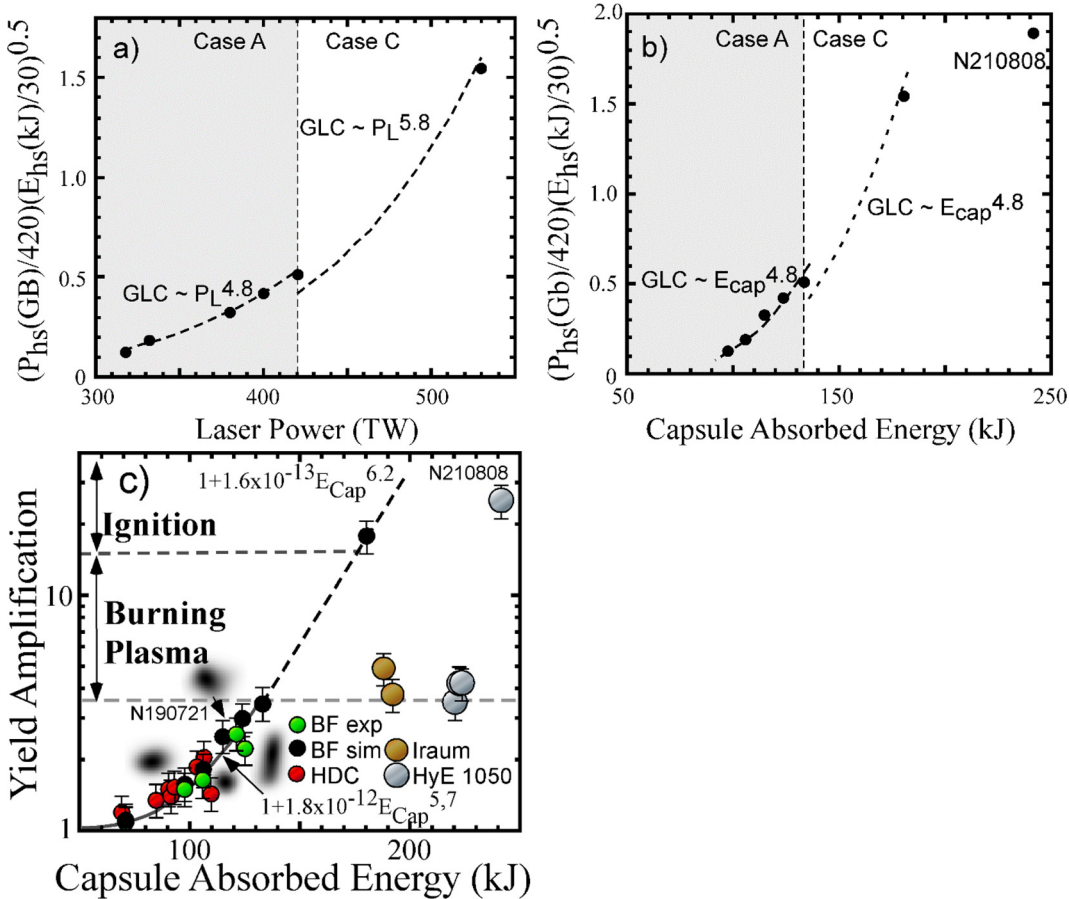


FIG. 5. Generalized Lawson criteria, $P_{hs}(E_{hs})^{0.5}$, as a function of (a) laser power overplotted with analytic scaling and (b) capsule-absorbed energy. (c) Yield amplification, Y_{amp} , as a function of laser energy for the four BigFoot layered implosions (green circles) carried out in the 5.4×10.13 mm size *Hohlraum* and simulations¹ (black circles) which extrapolate the performance to higher laser energies. The neutron-based hotspot shapes measured in each of the experiments are plotted next to inferred yield amplifications. Also included are the two Iraum, brown circles, and HyE 1050, gray circles, shots which recently crossed the burning plasma threshold with 400–500 kJ more effective energy.

($Y_{amp} > 3.5$) at a laser energy of 1.5 MJ (430 TW) and reach ignition with capsule-absorbed energy ~ 175 kJ, using ~ 1.8 MJ of laser energy into a gold-lined *Hohlraum* equipped with 3.45 mm LEHs, and appropriately thicker fuel and ablator.^{3,4,12} With the typical NIF laser energy of 1.85 MJ and Au-lined DU *Hohlraums* with 3.1 mm LEHs, this platform could drive these capsules with up to 200 kJ of capsule-absorbed energy for these 844 μ m inner radius capsules.

The generalized Lawson criterion (GLC) has been used in both direct and indirect drives to determine the proximity of an implosion to ignition. Conveniently, the GLC, excluding alpha heating, scales as the square root of the ignition metric $E_{hs}P_{hs}^2$ derived previously,^{30,60}

$$GLC(P_{hs}, E_{hs}) = P_{hs}(Gbar/280)(E_{hs}(kJ/4))^{0.5}. \quad (21)$$

So, it follows that the 500 TW design using an Au-lined U *Hohlraum* on the lowest row of Table II promises a $\sqrt{3.6} = 1.9 \times$ higher GLC in 1D than shot N190721. Furthermore, published 1D simulations provide the relationship between Y_{amp} and GLC, in this case, for an

idealized BigFoot design as vary peak power, as shown by the black points and fitted curve in Fig. 6. So, scaling from the measured $Y_{amp} = 2.6$ of N190721 on that curve, the green point, that happens to be at $GLC \approx 0.62$, we predict a Y_{amp} of ≈ 18 for a 500 TW extrapolation that corresponds to a GLC that is $\sqrt{3.6}$ higher, at 1.18. This is consistent with the 500 TW simulation Y_{amp} of 17 in Fig. 4. One can also rewrite the neutron yield in terms of the yield amplification and peak power as follows:

$$Y \sim Y_{amp} n_i^2 T_i^{3.5} R_{hs}^3 \tau_{bw} \sim Y_{amp} T_r^{11} \sim Y_{amp} P_L^{3.2} \approx Y_{amp} P_{hs}^2, \quad (22)$$

where the DT fusion reaction rate $\sim T_i^{3.5}$, $R_{hs} \sim 1/T_r^{0.45}$ per Eqs. (14) and (18) and for the given design and per 1D simulations $T_i \sim T_r^{3.3}$ and $\tau_{bw} \sim 1/T_r^{3.5}$. Hence given the N190721 yield of 1.1×10^{16} , a 500 TW (530 TW effective given Au-lined DU) design yield extrapolates using Table II and Eq. (22) to $1.1 \times 10^{16} \times 18/2.6 \times (530/400)^{3.2} = 1.9 \times 10^{17}$ or 0.5 MJ, all else equal.

The analytic scaling for pressure and energy, without-alpha heating, along with the pressure and energy amplification scalings can

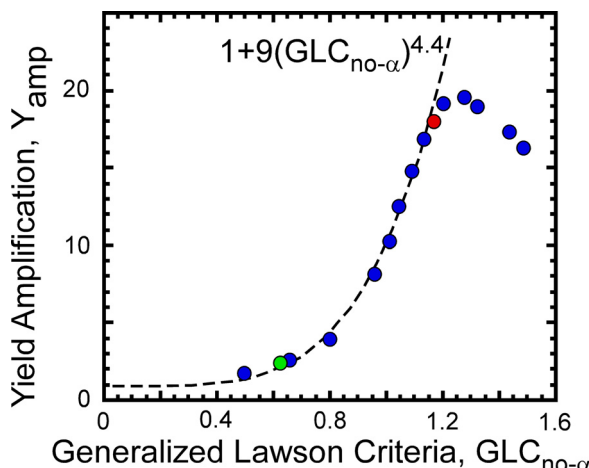


FIG. 6. Yield amplification vs no-alpha GLC from 1D full-scale Bigfoot simulations (black) on which is overlaid measured Y_{amp} of N190721 (green point) and 500 TW design at $\sqrt{\text{GLC}} = \sqrt{3}$ higher per Table II (red point).

then be compared to the GLC (with alpha heating) = $P_{\text{hs}}(E_{\text{hs}})^{0.5}$ from the BigFoot simulations. In particular, the P_{hs} , $P_{\text{hs-amp}}$, E_{hs} , and $E_{\text{hs-amp}}$ scaling with laser power for case A of $P_L^{17/7}$, $P_L^{0.8}$, $P_L^{11/7}$, and $P_L^{1.5}$, respectively, leads to a case A GLC (with-alpha heating) $\sim P_L^{4.8}$. This is in excellent agreement with the fit of the simulated BigFoot results shown in Fig. 5(a) of $\text{GLC} \sim P_L^5$. Likewise, the P_{hs} , $P_{\text{hs-amp}}$, E_{hs} , and $E_{\text{hs-amp}}$ scaling with laser power for case C of $P_L^{9.5/7}$, $P_L^{1.5}$, $P_L^{8/7}$, and $P_L^{4.7}$, respectively, leads to a case C GLC (with-alpha heating) $\sim P_L^{5.8}$. This is in reasonable agreement with the fit of the simulated BigFoot results shown in Fig. 5(a) of $\text{GLC} \sim P_L^{5.1}$. Again, using the relationship between P_L and E_{cap} from Fig. 2(c), we arrive at the analytic scalings

for GLC as a function of E_{cap} for case A of $\text{GLC} \sim E_{\text{cap}}^{4.8}$ and for case C which is also $\text{GLC} \sim E_{\text{cap}}^{4.8}$. This is then in reasonable agreement with the scalings in Fig. 5(b) for case A of $\text{GLC} \sim E_{\text{cap}}^{4.8}$ and for case C which is also $\text{GLC} \sim E_{\text{cap}}^{3.9}$. Figure 5(c) then shows the yield amplifications as a function of capsule-absorbed energy for the BigFoot experimental data (green circles) and simulations (black circles), the HDC data (red circles), and the best performing Iraum (brown circles) and HyE (gray circles) implosions. The yield amplification scalings for the BigFoot simulations in case A, $Y_{\text{amp}} \sim 1 + 1.8 \times 10^{-12} E_{\text{cap}}^{5.7}$ and case C, $Y_{\text{amp}} \sim 1 + 1.6 \times 10^{-13} E_{\text{cap}}^{6.2}$, show similar power scalings with capsule-absorbed energy. Again, by plotting the yield amplification as a function of capsule-absorbed energy, we can see that both the BigFoot and HDC implosions using $844 \mu\text{m}$ I.R. HDC capsules have a similar performance of yield amplification vs capsule-absorbed energy and are more efficient (lower E_{cap}) at reaching a given yield amplification level than the larger best performing Iraum ($1000 \mu\text{m}$ I.R.) and HyE ($1050 \mu\text{m}$ I.R.) campaigns. The ignition threshold, $\text{GLC} = 1$, is plotted for the BigFoot simulations suggesting that the ignition threshold could be reached with a capsule-absorbed energy $\sim 175 \text{ kJ}$, $\sim 1.8 \text{ MJ}$ of laser energy into a gold-lined *Hohlaum* with 3.45 mm LEHs. One could further improve the GLC and, hence, Y_{amp} and yield of the 500 TW BF 844 design by reducing the LEH size to 3.1 mm to improve the coupling by 6%, P_{hs} by 10%, GLC by $\approx 10\%$, Y_{amp} to its maximum simulated value of 20, shown in Fig. 6, for this design adiabat and yield 0.7 MJ . However, more impactful options potentially exist: lengthening the laser pulse to optimize the shock timing for reduced adiabat (employed by the HDC 844 campaign) or better quality more highly doped capsules to reduce mix and reduce the adiabat to increase the compression, confinement time, and $Y_{\text{amp}}(>30)$ and increasing the DT fuel layer thickness to further increase the fuel areal density and the achievable burn-up fraction and maximum Y_{amp} as discussed next.

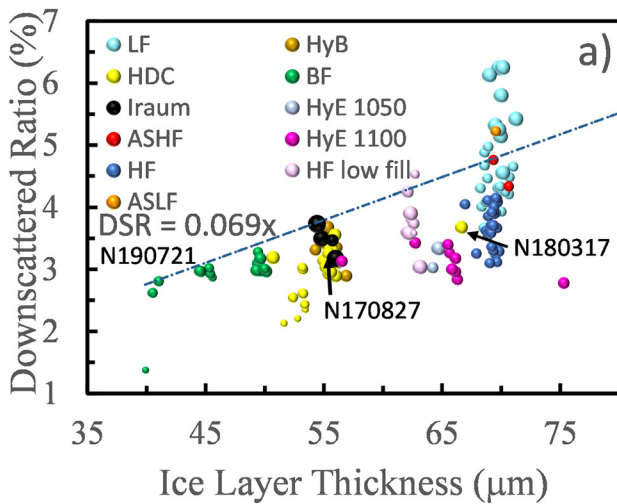
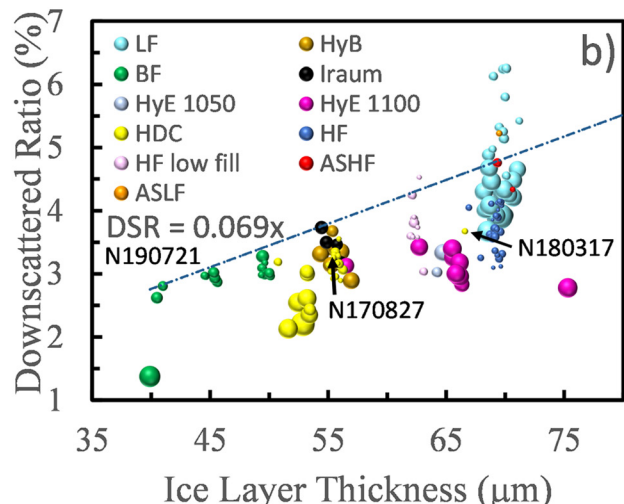


FIG. 7. Down-scattered ratio (DSR) vs initial ice thickness for most campaigns on the NIF. (a) The point size is proportional to the percent of dopant in the ablator, W dopant for the HDC ablator campaigns (BF, HDC, Iraum, HyB, HyE1100, and HyE1050) and Si for the CH ablator campaigns (LF, HF, ASHF, and HF low fill).



VIII. STAGNATED FUEL AREAL DENSITY

In this section, we compare the DSRs from many of the campaigns on the NIF, sorted by the initial ice thickness and further sorted by dopant level and coast time in Figs. 7(a) and 7(b). Only shots with $Y_{\text{amp}} < 3$ are plotted as the DSR is expected to drop slowly with increasing yield amplification (by $\simeq 4\%$ at $Y_{\text{amp}} = 3$) as alpha-heating leads to an explosion phase before peak burn. The residual DSR variations within a given campaign or between campaigns can be attributed to variations in delivered shock strength and timing affecting adiabat,^{61,62} level of modes 1 and 2 drive asymmetries,^{63,64} dopant areal density [as depicted by the size of circles in Fig. 7(a)] affecting Atwood # at the interface and, hence, level of fuel/ablator mix, coast time⁶⁵ [depicted by the size of circles in Fig. 7(b)], level of multi-keV x-ray preheat spectrum set by peak laser intensity, *Hohlraum* wall material⁶⁶ and *Hohlraum* temperature, *Hohlraum* geometry,^{56,67} and potential level of > 170 keV hot electrons preheating the inner ablator layer and the fuel.⁶⁸

A. Thicker DT ice

In Refs. 3 and 4, it was pointed out that the DSR between experiments carried out on two different platforms with two separate ablator materials had measured maximum experimental DSRs that were proportional to the initial ice thickness. We have extended that in Figs. 7(a) and 7(b) to include the DSR achieved on many platforms conducted on the NIF, including both HDC and CH implosions. This figure shows that the maximum DSR increases with increasing initial DT fuel thickness. As such, thickening the DT fuel can be an important way to increase the burn-up fraction in layered implosions and lead to higher performance.^{3,4} The fractional burn-up of the fuel, ϕ , in a robustly igniting ICF plasma can be represented² by $\phi = \rho r / (\rho r + \rho r_B(T_{\text{ion}}))$, where ρr is the total areal density of the imploded mass of fuel and remaining ablator and $\rho r_B(T_{\text{burn}})$ is a decreasing function of T_{ion} , asymptoting to 6 g/cm^2 .

To directly measure the effect of a thicker ice layer on DSR, a comparison experiment, N180317, was carried out in the HDC platform where the ice thickness was increased by 11.6, 66.6 vs 55 μm , over four other experiments repeating N170827. The pulse shape on N170827 and repeats was lengthened on N180317 to keep the shock timing the same through the thicker ice layer and maintain a similar velocity between the experiments. The DSR measured in the two sets of experiments increased from 3.13 ± 0.2 to 3.68 ± 0.2 , increasing by 18% as the DT ice layer was increased by 21%. The velocity of the two experiments was estimated to be the same within error bars,

$408 \pm 10 \text{ km/s}$ on N170827 to $404 \pm 10 \text{ km/s}$ on N180317. The bang time increased from 8.18 to 8.66 ns, consistent with the expected 0.4 ns increase in the laser pulse lengths, 7.8 vs 8.2 ns, needed to maintain the shock symmetry through the thicker ice layer.

In the set of four layered implosions that were performed in the BigFoot 844 platform in the $5.4 \times 10.13 \text{ mm}$ *Hohlraum*, the ablator thickness and ice thickness were increased on the latter two shots relative to the initial two while keeping the *Hohlraum* and the capsule inner radius fixed as detailed in Table III. For these two latter shots, the ice thickness was increased by 9.3%, the ablator thickness by 5.9%, and the laser energy increased from 1.1 to 1.33 MJ relative to the previous two implosions in this platform. The average DSR for the two shots with the thicker ice/ablator increased by 11.6% per Table III. However, the higher DSR was partially due to a 5% higher velocity, a 3% effect assuming $\text{DSR} \sim v_{\text{imp}}^{0.6}$. In addition, across all the BigFoot implosions, 844 and 950 scales, there were roughly three ice layer thicknesses employed: 40, 45, and 50 μm . As seen in Figs. 7(a) and 7(b) at each of these ice thicknesses, the peak DSR falls close to the dashed line, $\text{DSR in \%} = 0.069 \times \text{ice thickness in } \mu\text{m}$.

Subsequent to these experiments, a variety of thicker DT ice layers spanning 57–76 μm were used in the HyE1100 campaign.^{44,45} The nanocrystalline high density carbon ablators, UNCD, used in these experiments had numerous internal defects, voids, and surface pits, whereas the internal voids at least were believed to be largely absent from the experiments described above (except for the HyB capsules) which used microcrystalline high density carbon capsules, MCD. These poorer quality nanocrystalline capsules likely contributed to the lower $\text{DSR}/(\mu\text{m of ice})$ seen in the HyB and HyE1100 campaigns by mixing more ablator material into the ice layer. Unlike BigFoot and HDC campaigns, the HyE1100 DSR did not vary with ice layer thickness for a given coast time, perhaps because of the poorer capsule quality. The yield of the implosions, however, increased by up to a factor of two with the thicker ice layer. Recently, nanocrystalline capsules with high dopant levels have been developed which are of much higher quality than the previous UNCD and MCD capsules and should lead to reduced mix and increased DSRs relative to the capsules used in earlier campaigns.

B. Coast time

Figure 7(b) shows that the DSRs within a given design increase as coast time decreases, as noted previously for subsets of the data shown here. The clearest examples are within the CH LF, CH HF, HDC, and HyB series where coast times varied significantly (from as low as 0.5 to

TABLE III. Measured data from the BigFoot 844 campaigns.

Shot or design	Laser energy (MJ)	Laser power (TW)	Ablator thickness (μm)	DT fuel thickness (μm)	Peak velocity ($\mu\text{m/ns}$)	Primary yield	Tion (keV)	DSR (%)	Neutron P0 (μm)	Hotspot pressure (Gbar)	Yield amp.
N161030	1.06	318	63.8	39.9	388	1.7×10^{15}	4.14	2.61	24.4	158	1.5
N170109	1.15	332	65.3	40.5	392	2.3×10^{15}	4.16	2.81	22.4	214	1.6
N190617	1.35	404	68.5	41.0	404	6.6×10^{15}	4.58	3.12	22.3	316	2.2
N190721	1.31	403	68.3	44.6	400	9.5×10^{15}	4.83	3.12	27.6	291	2.5

as high as 2 ns). The optimum use of a given laser energy and power would leave the laser drive on until just before deceleration time, so typically a coast time of 0.5 ns before bang time, scaling with capsule size/peak velocity, as assumed in Secs. IV–VII. Long coast times, >1.2 ns, were present in the HyE 1100 and HyB campaigns due to their larger capsules, *Hohlraums*, and LEHs, leading to lower DSR values. Therefore, the use of a smaller hotter *Hohlraum* and capsule should also relax the requirements on laser energy required to maintain short coast times.

C. Design adiabat

The no-alpha heating DSR²⁶ is also expected to depend on the adiabat and velocity of the implosion according to $DSR \sim \alpha^{-0.8} V_{imp}^{0.6}$. Indeed, the highest DSR/(thickness of ice) is seen for the CH LowFoot (LF) shots (teal points) which have a significantly lower design adiabat <1.6 than the other campaigns and, hence, higher convergence. A case where two different campaigns can be compared to look at the effect of adiabat on compression is the adiabat-shaped high foot and the high foot campaigns. In the adiabat-shaped high foot campaign (red points), the trough was lower relative to the high foot campaign (blue points), which allowed the first shock to decay as it traveled through the ablator and enter the DT ice layer at a lower velocity than the high foot campaign and, hence, led to a lower adiabat and higher compression.^{53,55} As shown in Figs. 7(a) and 7(b), the peak DSR in the adiabat shaping campaign was ~15% higher than in the high foot campaign with equivalent capsule dopant, similar implosion velocity, and coast time.

While going to lower adiabat has led to higher compression and DSR in plastic implosions, this has not been as apparent in the HDC ablator implosions. Given the DSR dependence on design adiabat, it would be expected that the BigFoot campaign would have a lower DSR/(thickness of ice) than most of the campaigns on the NIF due to its higher design adiabat, $\alpha = 4$. However, what is seen in Fig. 7 is a linear relationship for the maximum DSR vs ice layer thickness across many of the platforms including the BigFoot (green points), Adiabat-Shaped High Foot (red points), Iraum (black points), Low-Fill High Foot (light gray points), and the HyB (brown points) implosions consistent with these platforms having a similar fuel convergence ratio despite their different design adiabats.²⁶ Though, the Iraum campaign's DSR/(μm of ice) is higher than the other campaigns on the NIF that used HDC ablators. The Iraum used both a higher picet power/energy, ~20%, and lower trough, ~27%, than the HyE campaigns⁶⁹ leading to a decaying radiation temperature in the *Hohlraum*⁶⁹ which could have contributed to the higher DSR performance in that campaign.⁷⁰ The adiabat-shaped low foot campaign (orange point) as seen in Figs. 7(a) and 7(b) also used a higher picet power than the $1 \times \text{Si}$ dopant level low foot shots (light blue points) and achieved a similar DSR, ~5% higher, though it had a lower coast time, ~150 ps. The yield and yield amplification for the adiabat-shaped low-foot implosion was higher than all of the low-foot layered implosions.^{54,55} This suggests that ablation front growth reduction via adiabat shaping, in this case, was not a large factor in improving DSR but led to higher performance by reducing feedthrough of localized engineering perturbations such as the tent scar and fill tube. The Iraum also had a much higher W areal density content than the other campaigns on the NIF that used HDC ablators as discussed in Sec. VIII D.

D. Dopant level

The level of dopant in the ablators may also play a role in the maximum achievable DSR in DT implosions.^{20,51,71} The dopant layer shields the undoped ablator layer in contact with the DT fuel layer from higher energy x rays, >1.8 keV, which allow it to be compressed to a higher density and makes the fuel-ablator interface more stable though the higher dopant level increases ablation front instability which if bad enough can also reduce the average DSR. The diameter of the circles in Fig. 7(a) is a function of the dopant areal densities. The diameter of the circles in the HDC campaigns is normalized to the areal density of W dopant where the smallest circle represents 0 μm % W dopant in the HDC capsules. The diameter of the circles in the CH campaigns is normalized to the atom percent of Si dopant where most of the circles represent 1 \times Si dopant in the CH capsules, which defines as 2% by atomic fraction Si in the most doped layer. The undoped HDC experiments had very low DSR values, as seen by the small yellow and green circles toward the bottom left of Fig. 7(a); although as seen in Fig. 7(b), these also corresponded to long coast times, up to 2 ns, which reduces the DSR. In addition, some of the more recent campaigns utilizing HDC ablators used higher tungsten dopant areal densities than the HDC and BigFoot campaigns. The Iraum campaign is the only HDC platform to match the maximum DSR/(μm of ice) of the BigFoot campaign, and it did so with longer coast times as seen in Fig. 7(b). Figure 7(a) shows that the Iraum capsules had much higher W dopant areal density, ρ_R , than the HyE 1050, BigFoot, and HDC capsules by 30%–40% and a slightly higher mass, 2%–4%, for their scale (thickness).⁶ Higher W dopant areal densities would likely help the other HDC campaigns achieve a higher value of DSR/(μm of ice).

Putting the full NIF energy into a smaller *Hohlraum* is expected to increase the radiation temperature relative to current *Hohlraums*. As stated, the radiation temperature could rise from 315 eV in the larger *Hohlraums* to 335 eV. Currently, the m-band fraction of the *Hohlraum* drive, x-ray energies >1.8 keV, is about 20%. The Planckian component of this m-band fraction at 315 eV is ~16.5%. At 335 eV, we would expect a Planckian component of ~20%. Thus, we would expect the m-band fraction to increase from ~20% to ~24% at the higher Tr which would require a small increase in the dopant areal density to account for the 20% increase in the number of x-rays above 1.8 keV as well as their higher fluence on the capsule due to the closer proximity of the outer beams to the capsule with the smaller size of the *Hohlraum*.

E. Hot electrons

Reduction of parametric instabilities, in particular, stimulated Raman scattering, and two plasmon decay which create hot electrons in the damping of the Langmuir waves could also be important in achieving higher DSRs. These hot electrons can deposit their energy into the ablator and the DT fuel making them more difficult to compress and lowering the achievable DSR for the implosion. This is one of the differences between the 1.6 mg/cc ^4He *Hohlraum* fill high foot CH campaign (blue points) and the 0.6 mg/cc *Hohlraum* fill high foot CH campaign (gray points) though the first low-fill high foot CH also had a lower first shock speed. The high and low gas-fill campaigns experienced SRS backscatter of 10%–15% and <1%, respectively, and the former also showed superhot electrons likely from two-plasmon

decay.⁶⁸ As seen in Fig. 7, the best-performing low-fill high-foot implosion had 15% higher DSR/(μms of ice) than the best-performing high-foot implosion for similar design adiabat and implosion velocity. It is not anticipated that the smaller *Hohlraums* at 0.3 mg/cc *Hohlraum* fill would see a higher percentage of SRS at higher laser energies. Moreover, the BigFoot campaign with its higher design adiabat would be less affected by the hot electrons than the lower design adiabat HDC campaign if the SRS/hot electron levels did increase.

IX. SUMMARY

Most efforts to improve the performance of layered implosions to date have focused on increasing the capsule size to increase the surface area and the capsule-absorbed energy. In this article, we expound upon our approach in Refs. 3 and 4 where we reduce the losses using a smaller *Hohlraum* to increase the radiation drive power. The higher drive enables comparable capsule-absorbed energy with smaller surface area capsules. By increasing the laser peak power, the higher T_r drive on the smaller capsule should enable both a higher hot spot generalized Lawson criterion and pressure than present for the larger capsules in larger *Hohlraums* driven with more energy. Specifically, from analytic scaling of the rocket model of implosions validated by simulations, the generalized Lawson criterion $\sim E_{\text{hs}}^{0.5} P_{\text{hs}}$ increases as $\approx P_{\text{L}}^{2.3}$ by almost 2 \times going from existing 400 TW implosions in a Au *Hohlraum* to the NIF 500 TW peak power limit in a higher albedo Au-lined U *Hohlraum*. This, in turn, should allow prior 844 implosions that reached a Y_{amp} of 2.5 to reach burning plasma and near ignition conditions (0.5–0.7 MJ), even with as little as 1.5–1.7 MJ of laser energy.

For further improvements, the ability to increase the fuel areal density and, hence, confinement time at stagnation is predicted to be critical in achieving a larger burn-up fraction of the assembled DT fuel and subsequently in achieving higher yields and performance. In this article, we also showed that the maximum DSR does increase with initial fuel thickness (ρR), for shots in which the shock timing and implosion velocity are kept fixed.

ACKNOWLEDGMENTS

We wish to thank the NIF operations team. This work was performed under the auspices of the U.S. Department of Energy by Lawrence Livermore National Laboratory under Contract No. DE-AC52-07NA27344 and General Atomics under contract No. DE-NA0001808. The data that support the findings of this study are available from the corresponding author upon reasonable request. This document was prepared as an account of work sponsored by an agency of the US government. Neither the US government nor Lawrence Livermore National Security, LLC, nor any of their employees makes any warranty, expressed or implied, or assumes any legal liability or responsibility for the accuracy, completeness, or usefulness of any information, apparatus, product, or process disclosed, or represents that its use would not infringe privately owned rights. Reference herein to any specific commercial product, process, or service by trade name, trademark, manufacturer, or otherwise does not necessarily constitute or imply its endorsement, recommendation, or favoring by the US government or Lawrence Livermore National Security, LLC. The views and opinions of authors expressed herein do not necessarily state or reflect those of

the US government or Lawrence Livermore National Security, LLC, and shall not be used for advertising or product endorsement purposes.

AUTHOR DECLARATIONS

Conflict of Interest

The authors have no conflicts to disclose.

Author Contributions

Kevin Baker: Conceptualization (equal); Formal analysis (equal); Investigation (equal); Writing – original draft (equal); Writing – review & editing (equal). **Debra Callahan:** Methodology (equal); Project administration (equal); Supervision (equal). **Ogden S. Jones:** Investigation (equal); Software (equal). **Laura Berzak Hopkins:** Conceptualization (equal); Investigation (equal); Software (equal). **Shahab Firasat Khan:** Data curation (equal); Investigation (equal). **Brian K. Spears:** Conceptualization (equal); Funding acquisition (equal); Investigation (equal). **Sebastien LePape:** Conceptualization (equal); Investigation (equal). **Nathan B. Meezan:** Conceptualization (equal); Investigation (equal); Software (equal). **Darwin D.-M Ho:** Methodology (equal); Software (equal). **Tilo Doeppner:** Data curation (equal); Investigation (equal). **Denise Hinkel:** Methodology (equal). **Cliff Thomas:** Conceptualization (equal); Formal analysis (equal); Investigation (equal); Software (equal). **Eduard Liviu Dewald:** Investigation (equal). **Riccardo Tommasini:** Investigation (equal). **Matthias Hohenberger:** Investigation (equal). **Christopher Weber:** Software (equal). **Daniel S. Clark:** Software (equal). **Douglas Tod Woods:** Software (equal). **Jose L. Milovich:** Software (equal). **David J. Strozzi:** Investigation (equal). **Andrea L. Kritcher:** Investigation (equal). **Harry F. Robey:** Investigation (equal). **Otto L. Landen:** Formal analysis (equal); Writing – review & editing (equal). **James S. Ross:** Investigation (equal). **Vladimir Smalyuk:** Investigation (equal). **Peter Andrew Amendt:** Investigation (equal). **Benjamin Bachmann:** Data curation (equal). **Laura Robin Benedetti:** Data curation (equal). **Richard Marshall Bionta:** Data curation (equal). **Peter M. Celliers:** Data curation (equal). **David N. Fittinghoff:** Data curation (equal). **Clement Goyon:** Investigation (equal). **Robert Hatarik:** Data curation (equal). **Steven W. Haan:** Methodology (equal). **Nobuhiko Izumi:** Investigation (equal). **Maria Gatu Johnson:** Data curation (equal). **George A. Kyrala:** Methodology (equal). **Tammy Ma:** Data curation (equal). **Kevin Meaney:** Data curation (equal). **Marius Millot:** Data curation (equal). **Sabrina Nagel:** Data curation (equal). **Pravesh K. Patel:** Funding acquisition (equal). **David Turnbull:** Data curation (equal). **Petr Volegov:** Data curation (equal). **John Lindl:** Methodology (equal). **Charles B. Yeamans:** Data curation (equal). **C. H. Wilde:** Data curation (equal). **Daniel T. Casey:** Conceptualization (equal); Formal analysis (equal); Investigation (equal). **Christopher V. Young:** Methodology (equal). **Ryan Nora:** Investigation (equal); Software (equal). **Omar A. Hurricane:** Methodology (equal); Project administration (equal); Supervision (equal).

DATA AVAILABILITY

The data that support the findings of this study are available from the corresponding author upon reasonable request.

REFERENCES

- ¹J. Lindl, *Phys. Plasmas* 2(11), 3933–4024 (1995).

- ²S. Atzeni and J. Meyer-ter-Vehn, *The Physics of Inertial Fusion* (Oxford University Press, 2008).
- ³K. L. Baker, C. A. Thomas, D. T. Casey, S. Khan, B. K. Spears, R. Nora, T. Woods, J. L. Milovich, R. L. Berger, D. Strozzi, D. Clark, M. Hohenberger, O. A. Hurricane, D. A. Callahan, O. L. Landen, B. Bachmann, R. Benedetti, R. Bionta, P. M. Celliers, D. Fittinghoff, C. Goyon, G. Grim, R. Hatarik, N. Izumi, M. Gatu Johnson, G. Kyrala, T. Ma, M. Millot, S. R. Nagel, A. Pak, P. K. Patel, D. Turnbull, P. L. Volegov, and C. Yeamans, *Phys. Rev. Lett.* **121**(13), 135001 (2018).
- ⁴K. L. Baker, "Increasing stagnation pressure," LLNL proposal, 2019.
- ⁵M. C. Herrmann, M. Tabak, and J. D. Lindl, *Nucl. Fusion* **41**, 99–111 (2001).
- ⁶K. L. Baker, O. Jones, C. Weber, D. Clark, P. K. Patel, C. A. Thomas, O. L. Landen, R. Nora, G. J. Anderson, J. Gaffney, S. MacLaren, D. T. Casey, T. Döppner, E. L. Dewald, R. Tommasini, B. K. Spears, J. Salmonson, M. Hohenberger, S. Khan, A. Zylstra, A. Kritch, P. Amendt, V. Smalyuk, J. Lindl, C. Young, J. S. Ross, D. Ho, O. A. Hurricane, D. A. Callahan, T. Woods, J. L. Milovich, D. J. Strozzi, B. Bachmann, R. Bionta, P. M. Celliers, D. Fittinghoff, R. Hatarik, M. Gatu Johnson, K. Meaney, M. Millot, P. L. Volegov, and C. Wilde, *Phys. Plasmas* **29**(6), 062705 (2022).
- ⁷K. L. Baker, S. MacLaren, O. Jones, B. K. Spears, P. K. Patel, R. Nora, L. Divol, O. L. Landen, G. J. Anderson, J. Gaffney, M. Kruse, O. A. Hurricane, D. A. Callahan, A. R. Christoperson, J. Salmonson, E. P. Hartouni, T. Döppner, E. Dewald, R. Tommasini, C. A. Thomas, C. Weber, D. Clark, D. T. Casey, M. Hohenberger, S. Khan, T. Woods, J. L. Milovich, R. L. Berger, D. Strozzi, A. Kritch, B. Bachmann, R. Benedetti, R. Bionta, P. M. Celliers, D. Fittinghoff, R. Hatarik, N. Izumi, M. Gatu Johnson, G. Kyrala, T. Ma, K. Meaney, M. Millot, S. R. Nagel, A. Pak, P. L. Volegov, C. Yeamans, and C. Wilde, *Phys. Rev. E* **107**(1), 015202 (2023).
- ⁸K. L. Baker, C. A. Thomas, D. T. Casey, M. Hohenberger, S. Khan, B. K. Spears, O. L. Landen, R. Nora, D. T. Woods, J. L. Milovich, R. L. Berger, D. Strozzi, C. Weber, D. Clark, O. A. Hurricane, D. A. Callahan, A. L. Kritch, B. Bachmann, L. R. Benedetti, R. Bionta, P. M. Celliers, D. Fittinghoff, C. Goyon, R. Hatarik, N. Izumi, M. Gatu Johnson, G. Kyrala, T. Ma, K. Meaney, M. Millot, S. R. Nagel, P. K. Patel, D. Turnbull, P. L. Volegov, C. Yeamans, and C. Wilde, *Phys. Rev. E* **102**(2–1), 023210 (2020).
- ⁹P. K. Patel, P. T. Springer, C. R. Weber, L. C. Jarrott, O. A. Hurricane, B. Bachmann, K. L. Baker, L. F. Berzak Hopkins, D. A. Callahan, D. T. Casey, C. J. Cerjan, D. S. Clark, E. L. Dewald, L. Divol, T. Döppner, J. E. Field, D. Fittinghoff, J. Gaffney, V. Geppert-Kleinrath, G. P. Grim, E. P. Hartouni, R. Hatarik, D. E. Hinkel, M. Hohenberger, K. Humbird, N. Izumi, O. S. Jones, S. F. Khan, A. L. Kritch, M. Kruse, O. L. Landen, S. Le Pape, T. Ma, S. A. MacLaren, A. G. MacPhee, L. P. Masse, N. B. Meezan, J. L. Milovich, R. Nora, A. Pak, J. L. Peterson, T. Ralph, H. F. Robey, J. D. Salmonson, V. A. Smalyuk, B. K. Spears, C. A. Thomas, P. L. Volegov, A. Zylstra, and M. J. Edwards, *Phys. Plasmas* **27**(5), 050901 (2020).
- ¹⁰D. T. Casey, C. A. Thomas, K. L. Baker, B. K. Spears, M. Hohenberger, S. F. Khan, R. C. Nora, C. R. Weber, D. T. Woods, O. A. Hurricane, D. A. Callahan, R. L. Berger, J. L. Milovich, P. K. Patel, T. Ma, A. Pak, L. R. Benedetti, M. Millot, C. Jarrott, O. L. Landen, R. M. Bionta, B. J. MacGowan, D. J. Strozzi, M. Stadermann, J. Biener, A. Nikroo, C. S. Goyon, N. Izumi, S. R. Nagel, B. Bachmann, P. L. Volegov, D. N. Fittinghoff, G. P. Grim, C. B. Yeamans, M. Gatu Johnson, J. A. Frenje, N. Rice, C. Kong, J. Crippen, J. Jaquez, K. Kangas, and C. Wild, *Phys. Plasmas* **25**(5), 056308 (2018).
- ¹¹C. A. Thomas, E. M. Campbell, K. L. Baker, D. T. Casey, M. Hohenberger, A. L. Kritch, B. K. Spears, S. F. Khan, R. Nora, D. T. Woods, J. L. Milovich, R. L. Berger, D. Strozzi, D. D. Ho, D. Clark, B. Bachmann, L. R. Benedetti, R. Bionta, P. M. Celliers, D. N. Fittinghoff, G. Grim, R. Hatarik, N. Izumi, G. Kyrala, T. Ma, M. Millot, S. R. Nagel, P. K. Patel, C. Yeamans, A. Nikroo, M. Tabak, M. Gatu Johnson, P. L. Volegov, and S. M. Finnegan, *Phys. Plasmas* **27**(11), 112705 (2020).
- ¹²C. A. Thomas, E. M. Campbell, K. L. Baker, D. T. Casey, M. Hohenberger, A. L. Kritch, B. K. Spears, S. F. Khan, R. Nora, D. T. Woods, J. L. Milovich, R. L. Berger, D. Strozzi, D. D. Ho, D. Clark, B. Bachmann, L. R. Benedetti, R. Bionta, P. M. Celliers, D. N. Fittinghoff, G. Grim, R. Hatarik, N. Izumi, G. Kyrala, T. Ma, M. Millot, S. R. Nagel, P. K. Patel, C. Yeamans, A. Nikroo, M. Tabak, M. Gatu Johnson, P. L. Volegov, and S. M. Finnegan, *Phys. Plasmas* **27**, 112712 (2020).
- ¹³C. A. Thomas, E. M. Campbell, K. L. Baker, D. T. Casey, M. Hohenberger, A. L. Kritch, B. K. Spears, S. F. Khan, R. Nora, D. T. Woods, J. L. Milovich, R. L. Berger, D. Strozzi, D. D. Ho, D. Clark, B. Bachmann, L. R. Benedetti, R. Bionta, P. M. Celliers, D. N. Fittinghoff, G. Grim, R. Hatarik, N. Izumi, G. Kyrala, T. Ma, M. Millot, S. R. Nagel, P. K. Patel, C. Yeamans, A. Nikroo, M. Tabak, M. Gatu Johnson, P. L. Volegov, and S. M. Finnegan, *Phys. Plasmas* **27**, 112708 (2020).
- ¹⁴M. Hohenberger, D. T. Casey, C. A. Thomas, O. L. Landen, K. L. Baker, L. R. Benedetti, D. A. Callahan, O. A. Hurricane, N. Izumi, S. F. Khan, T. Ma, D. A. Mariscal, S. R. Nagel, A. Pak, and B. K. Spears, *Phys. Plasmas* **26**(11), 112707 (2019).
- ¹⁵R. Berger, C. A. Thomas, K. Baker, D. Casey, C. Goyon, J. Park, N. Lemos, S. Khan, M. Hohenberger, J. Milovich, D. Strozzi, M. Belyaev, T. Chapman, and A. B. Langdon, *Phys. Plasmas* **26**, 012709 (2019).
- ¹⁶A. J. MacKinnon, N. B. Meezan, J. S. Ross, S. Le Pape, L. Berzak Hopkins, L. Divol, D. Ho, J. Milovich, A. Pak, J. Ralph, T. Döppner, P. K. Patel, C. Thomas, R. Tommasini, S. Haan, A. G. MacPhee, J. McNaney, J. Caggiano, R. Hatarik, R. Bionta, T. Ma, B. Spears, J. R. Rygg, L. R. Benedetti, R. P. J. Town, D. K. Bradley, E. L. Dewald, D. Fittinghoff, O. S. Jones, H. R. Robey, J. D. Moody, S. Khan, D. A. Callahan, A. Hamza, J. Biener, P. M. Celliers, D. G. Braun, D. J. Erskine, S. T. Prisbrey, R. J. Wallace, B. Kozioziemski, R. Dylla-Spears, J. Sater, G. Collins, E. Storm, W. Hsing, O. Landen, J. L. Atherton, J. D. Lindl, M. J. Edwards, J. A. Frenje, M. Gatu-Johnson, C. K. Li, R. Petrasco, H. Rinderknecht, M. Rosenberg, F. H. Séguin, A. Zylstra, J. P. Knauer, G. Grim, N. Guler, F. Merrill, R. Olson, G. A. Kyrala, J. D. Kilkenny, A. Nikroo, K. Moreno, D. E. Hoover, C. Wild, and E. Werner, *Phys. Plasmas* **21**(5), 056318 (2014).
- ¹⁷S. Le Pape, L. F. Berzak Hopkins, L. Divol, A. Pak, E. L. Dewald, S. Bhandarkar, L. R. Benedetti, T. Bunn, J. Biener, J. Crippen, D. Casey, D. Edgell, D. N. Fittinghoff, M. Gatu-Johnson, C. Goyon, S. Haan, R. Hatarik, M. Havre, D. D. Ho, N. Izumi, J. Jaquez, S. F. Khan, G. A. Kyrala, T. Ma, A. J. Mackinnon, A. G. MacPhee, B. J. MacGowan, N. B. Meezan, J. Milovich, M. Millot, P. Michel, S. R. Nagel, A. Nikroo, P. Patel, J. Ralph, J. S. Ross, N. G. Rice, D. Strozzi, M. Stadermann, P. Volegov, C. Yeamans, C. Weber, C. Wild, D. Callahan, and O. A. Hurricane, *Phys. Rev. Lett.* **120**(24), 245003 (2018).
- ¹⁸L. F. Berzak Hopkins, N. B. Meezan, S. Le Pape, L. Divol, A. J. Mackinnon, D. D. Ho, M. Hohenberger, O. S. Jones, G. Kyrala, J. L. Milovich, A. Pak, J. E. Ralph, J. S. Ross, L. R. Benedetti, J. Biener, R. Bionta, E. Bond, D. Bradley, J. Caggiano, D. Callahan, C. Cerjan, J. Church, D. Clark, T. Doppner, R. Dylla-Spears, M. Eckart, D. Edgell, J. Field, D. N. Fittinghoff, M. Gatu Johnson, G. Grim, N. Guler, S. Haan, A. Hamza, E. P. Hartouni, R. Hatarik, H. W. Herrmann, D. Hinkel, D. Hoover, H. Huang, N. Izumi, S. Khan, B. Kozioziemski, J. Kroll, T. Ma, A. MacPhee, J. McNaney, F. Merrill, J. Moody, A. Nikroo, P. Patel, H. F. Robey, J. R. Rygg, J. Sater, D. Sayre, M. Schneider, S. Sepke, M. Stadermann, W. Stoeffl, C. Thomas, R. P. Town, P. L. Volegov, C. Wild, C. Wilde, E. Woerner, C. Yeamans, B. Yoxall, J. Kilkenny, O. L. Landen, W. Hsing, and M. J. Edwards, *Phys. Rev. Lett.* **114**(17), 175001 (2015).
- ¹⁹N. B. Meezan, L. F. Berzak Hopkins, S. Le Pape, L. Divol, A. J. MacKinnon, T. Döppner, D. D. Ho, O. S. Jones, S. F. Khan, T. Ma, J. L. Milovich, A. Pak, J. S. Ross, C. A. Thomas, L. R. Benedetti, D. K. Bradley, P. M. Celliers, D. S. Clark, J. E. Field, S. W. Haan, N. Izumi, G. A. Kyrala, J. D. Moody, P. K. Patel, J. E. Ralph, J. R. Rygg, S. M. Sepke, B. K. Spears, R. Tommasini, R. P. J. Town, J. Biener, R. M. Bionta, E. J. Bond, J. A. Caggiano, M. J. Eckart, M. Gatu Johnson, G. P. Grim, A. V. Hamza, E. P. Hartouni, R. Hatarik, D. E. Hoover, J. D. Kilkenny, B. J. Kozioziemski, J. J. Kroll, J. M. McNaney, A. Nikroo, D. B. Sayre, M. Stadermann, C. Wild, B. E. Yoxall, O. L. Landen, W. W. Hsing, and M. J. Edwards, *Phys. Plasmas* **22**(6), 062703 (2015).
- ²⁰D. M. Ho, S. W. Haan, J. D. Salmonson, D. S. Clark, J. D. Lindl, J. L. Milovich, C. A. Thomas, L. F. Berzak Hopkins, and N. B. Meezan, *J. Phys.: Conf. Ser.* **717**, 012023 (2016).
- ²¹L. Divol, A. Pak, L. F. Berzak Hopkins, S. L. Pape, N. B. Meezan, E. L. Dewald, D. D. M. Ho, S. F. Khan, A. J. MacKinnon, J. S. Ross, D. P. Turnbull, C. Weber, P. M. Celliers, M. Millot, L. R. Benedetti, J. E. Field, N. Izumi, G. A. Kyrala, T. Ma, S. R. Nagel, J. R. Rygg, D. Edgell, A. G. MacPhee, C. Goyon, M. Hohenberger, B. J. MacGowan, P. Michel, D. Strozzi, W. S. Cassata, D. Casey, D. N. Fittinghoff, N. Gharibyan, R. Hatarik, D. Sayre, P. Volegov, C. Yeamans, B. Bachmann, T. Döppner, J. Biener, J. Crippen, C. Choate, H. Huang, C. Kong, A. Nikroo, N. G. Rice, M. Stadermann, S. D. Bhandarkar, S. Haan, B.

- Kozioziemski, W. W. Hsing, O. L. Landen, J. D. Moody, R. P. J. Town, D. A. Callahan, O. A. Hurricane, and M. J. Edwards, *Phys. Plasmas* **24**(5), 056309 (2017).
- ²²J. D. Lindl, P. Amendt, R. L. Berger, S. G. Glendinning, S. H. Glenzer, S. W. Haan, R. L. Kauffman, O. L. Landen, and L. J. Suter, *Phys. Plasmas* **11**(2), 339–491 (2004).
- ²³D. H. Cohen, O. L. Landen, and J. J. MacFarlane, *Phys. Plasmas* **12**, 122703 (2005).
- ²⁴G. B. Zimmerman and W. L. Krueer, *Comments Plasma Phys. Controlled Fusion* **2**, 51–60 (1975).
- ²⁵J. A. Harte, W. E. Alley, D. S. Bailey, J. L. Eddleman, and G. B. Zimmerman, “LASNEX—A 2-D physics code for modeling ICF,” Report No. UCRL-LR-105821-96-4 (Lawrence Livermore National Laboratory, 1996).
- ²⁶O. L. Landen, J. D. Lindl, S. W. Haan, D. T. Casey, P. M. Celliers, D. N. Fittinghoff, N. Gharibyan, V. N. Goncharov, G. P. Grim, E. P. Hartouni, O. A. Hurricane, B. J. MacGowan, S. A. MacLaren, K. D. Meaney, M. Millot, J. L. Milovich, P. K. Patel, H. S. Robey, P. T. Springer, P. L. Volegov, and M. J. Edwards, *Phys. Plasmas* **28**(4), 042705 (2021).
- ²⁷R. E. Olson, G. A. Rochau, O. L. Landen, and R. J. Leeper, *Phys. Plasmas* **18**, 032706 (2011).
- ²⁸A. Casner, T. Jalinaud, L. Masse, and D. Galmiche, *Phys. Plasmas* **22**, 100702 (2015).
- ²⁹N. B. Meezan, A. J. MacKinnon, D. G. Hicks, E. L. Dewald, R. Tommasini, S. Le Pape, T. Döppner, T. Ma, D. R. Farley, D. H. Kalantar, P. D. Nicola, D. A. Callahan, H. F. Robey, C. A. Thomas, S. T. Prisbrey, O. S. Jones, J. L. Milovich, D. S. Clark, D. C. Eder, M. B. Schneider, K. Widmann, J. A. Koch, J. D. Salmonson, Y. P. Opachich, L. R. Benedetti, S. F. Khan, A. G. MacPhee, S. M. Glenn, D. K. Bradley, E. G. Dzenitish, B. R. Nathan, J. J. Kroll, A. V. Hamza, S. N. Dixit, L. J. Atherton, O. L. Landen, S. H. Glenzer, W. W. Hsing, L. J. Suter, M. J. Edwards, B. J. MacGowan, E. I. Moses, R. E. Olson, J. L. Kline, G. A. Kyrala, A. S. Moore, J. D. Kilkenny, A. Nikroo, K. Moreno, and D. E. Hoover, *Phys. Plasmas* **20**(5), 056311 (2013).
- ³⁰J. D. Lindl, S. W. Haan, O. L. Landen, A. R. Christopherson, and R. Betti, *Phys. Plasmas* **25**(12), 122704 (2018).
- ³¹R. Betti, M. Umansky, V. Lobatchev, V. N. Goncharov, and R. L. McCrory, *Phys. Plasmas* **8**, 5257 (2001).
- ³²R. Betti, K. Anderson, V. N. Goncharov, R. L. McCrory, D. D. Meyerhofer, S. Skupsky, and R. P. J. Town, *Phys. Plasmas* **9**(5), 2277–2286 (2002).
- ³³J. D. Lindl, S. W. Haan, and O. L. Landen, *Phys. Plasmas* **30**, 012705 (2023).
- ³⁴O. A. Hurricane, D. A. Callahan, D. T. Casey, P. M. Celliers, C. Cerjan, E. L. Dewald, T. R. Dittrich, T. Döppner, D. E. Hinkel, L. F. B. Hopkins, J. L. Kline, S. Le Pape, T. Ma, A. G. MacPhee, J. L. Milovich, A. Pak, H. S. Park, P. K. Patel, B. A. Remington, J. D. Salmonson, P. T. Springer, and R. Tommasini, *Nature* **506**, 343–348 (2014).
- ³⁵P. K. Patel, “Hotspot model extended to burning plasmas and EP2,” *Phys. Plasmas* (submitted) (2023).
- ³⁶Y. Saillard, *Nucl. Fusion* **46**(12), 1017–1035 (2006).
- ³⁷J. L. Kline, D. A. Callahan, S. H. Glenzer, N. B. Meezan, J. D. Moody, D. E. Hinkel, O. S. Jones, A. J. Mackinnon, R. Benedetti, R. L. Berger, D. Bradley, E. L. Dewald, I. Bass, C. Bennett, M. Bowers, G. Brunton, J. Bude, S. Burkhardt, A. Condor, J. M. D. Nicola, P. D. Nicola, S. N. Dixit, T. Doeppner, E. G. Dzenitish, G. Erbert, J. Folta, G. Grim, S. Glenn, A. Hamza, S. W. Haan, J. Heebner, M. Henesian, M. Hermann, D. G. Hicks, W. W. Hsing, N. Izumi, K. Jancaitis, O. S. Jones, D. Kalantar, S. F. Khan, R. Kirkwood, G. A. Kyrala, K. Lafontaine, O. L. Landen, L. Lagin, D. Larson, S. L. Pape, T. Ma, A. G. MacPhee, P. A. Michel, P. Miller, M. Montincelli, A. S. Moore, A. Nikroo, M. Nostrand, R. E. Olson, A. Pak, H. S. Park, J. P. Patel, L. Pelz, J. Ralph, S. P. Regan, H. F. Robey, M. D. Rosen, J. S. Ross, M. B. Schneider, M. Shaw, V. A. Smalyuk, D. J. Strozzi, T. Suratwala, L. J. Suter, R. Tommasini, R. P. J. Town, B. Van Wonterghem, P. Wegner, K. Widmann, C. Widmayer, H. Wilkens, E. A. Williams, M. J. Edwards, B. A. Remington, B. J. Macgowan, J. D. Kilkenny, J. D. Lindl, L. J. Atherton, S. H. Batha, and E. Moses, *Phys. Plasmas* **20**, 056314 (2013).
- ³⁸J. Lindl, O. Landen, J. Edwards, and E. Moses, *Phys. Plasmas* **21**(2), 020501 (2014).
- ³⁹T. Döppner, D. E. Hinkel, L. C. Jarrott, L. Masse, J. E. Ralph, L. R. Benedetti, B. Bachmann, P. M. Celliers, D. T. Casey, L. Divol, J. E. Field, C. Goyon, R. Hatarik, M. Hohenberger, N. Izumi, S. F. Khan, A. L. Kritcher, T. Ma, B. J. MacGowan, M. Millot, J. Milovich, S. Nagel, A. Pak, J. Park, P. Patel, R. Tommasini, P. Volegov, C. Weber, O. L. Landen, D. A. Callahan, O. A. Hurricane, and M. J. Edwards, *Phys. Plasmas* **27**(4), 042701 (2020).
- ⁴⁰D. A. Callahan, O. A. Hurricane, J. E. Ralph, C. A. Thomas, K. L. Baker, L. R. Benedetti, L. F. Berzak Hopkins, D. T. Casey, T. Chapman, C. E. Czajka, E. L. Dewald, L. Divol, T. Döppner, D. E. Hinkel, M. Hohenberger, L. C. Jarrott, S. F. Khan, A. L. Kritcher, O. L. Landen, S. LePape, S. A. MacLaren, P. L. Masse, N. B. Meezan, A. E. Pak, J. D. Salmonson, D. T. Woods, N. Izumi, T. Ma, D. A. Mariscal, S. R. Nagel, J. L. Kline, G. A. Kyrala, E. N. Loomis, S. A. Yi, A. B. Zylstra, and S. H. Batha, *Phys. Plasmas* **25**(5), 056305 (2018).
- ⁴¹N. Izumi, D. T. Woods, N. B. Meezan, J. D. Moody, O. L. Landen, L. Divol, H. Chen, D. A. Callahan, M. Hohenberger, A. L. Kritcher, D. T. Casey, M. D. Rosen, J. S. Ross, M. B. Schneider, M. J. Edwards, and W. W. Hsing, *Phys. Plasmas* **28**(2), 022706 (2021).
- ⁴²R. E. Turner, P. Amendt, O. L. Landen, S. G. Glendinning, P. Bell, C. Decker, B. A. Hammel, D. Kalantar, D. Lee, R. Wallace, D. Bradley, M. Cable, R. S. Craxton, R. Kremens, W. Seka, J. Schnittman, K. Thorp, T. J. Murphy, N. Delamater, C. W. Barnes, A. Hauer, G. Magelssen, and J. Wallace, *Phys. Plasmas* **7**(1), 333–337 (2000).
- ⁴³J. E. Ralph, P. Michel, B. J. MacGowan, D. J. Strozzi, N. B. Meezan, J. M. Di Nicola, J. E. Heebner, V. J. Hernandez, L. Pelz, S. Yang, N. Lemos, L. Divol, A. Kemp, T. Chapman, S. F. Khan, O. L. Landen, J. D. Moody, R. P. J. Town, and M. J. Edwards, *Phys. Rev. Applied* **18**, 044040 (2022).
- ⁴⁴A. B. Zylstra, A. L. Kritcher, O. A. Hurricane, D. A. Callahan, K. Baker, T. Braun, D. T. Casey, D. Clark, K. Clark, T. Döppner, L. Divol, D. E. Hinkel, M. Hohenberger, C. Kong, O. L. Landen, A. Nikroo, A. Pak, P. Patel, J. E. Ralph, N. Rice, R. Tommasini, M. Schoff, M. Stadermann, D. Strozzi, C. Weber, C. Young, C. Wild, R. P. J. Town, and M. J. Edwards, *Phys. Rev. Lett.* **126**, 025001 (2021).
- ⁴⁵A. L. Kritcher, A. B. Zylstra, D. A. Callahan, O. A. Hurricane, C. Weber, J. Ralph, D. T. Casey, A. Pak, K. Baker, B. Bachmann, S. Bhandarkar, J. Biener, R. Bionta, T. Braun, M. Bruhn, C. Choate, D. Clark, J. M. Di Nicola, L. Divol, T. Doeppner, V. Geppert-Kleinrath, S. Haan, J. Heebner, V. Hernandez, D. Hinkel, M. Hohenberger, H. Huang, C. Kong, S. Le Pape, D. Mariscal, E. Marley, L. Masse, K. D. Meaney, M. Millot, A. Moore, K. Newman, A. Nikroo, P. Patel, L. Pelz, N. Rice, H. Robey, J. S. Ross, M. Rubery, J. Salmonson, D. Schlossberg, S. Sepke, K. Sequoia, M. Stadermann, D. Strozzi, R. Tommasini, P. Volegov, C. Wild, S. Yang, C. Young, M. J. Edwards, O. Landen, R. Town, and M. Herrmann, *Phys. Plasmas* **28**(7), 072706 (2021).
- ⁴⁶A. L. Kritcher, D. T. Casey, C. A. Thomas, A. B. Zylstra, M. Hohenberger, K. Baker, S. Le Pape, B. Bachmann, S. Bhandarkar, J. Biener, T. Braun, D. Clark, L. Divol, T. Döppner, D. Hinkel, C. Kong, D. Mariscal, M. Millot, J. Milovich, A. Nikroo, A. Pak, N. Rice, H. Robey, M. Stadermann, J. Sevier, D. Strozzi, C. Weber, C. Wild, B. Woodworth, J. Edwards, D. A. Callahan, and O. A. Hurricane, *Phys. Plasmas* **27**(5), 052710 (2020).
- ⁴⁷M. Hohenberger, D. T. Casey, A. L. Kritcher, A. Pak, A. B. Zylstra, C. A. Thomas, K. L. Baker, S. Le Pape, B. Bachmann, R. L. Berger, J. Biener, D. S. Clark, L. Divol, T. Döppner, V. Geppert-Kleinrath, D. Hinkel, H. Huang, C. Kong, O. L. Landen, J. Milovich, A. Nikroo, N. Rice, H. Robey, M. Schoff, J. Sevier, K. Sequoia, M. Stadermann, D. Strozzi, P. L. Volegov, C. Weber, C. Wild, B. Woodworth, D. A. Callahan, and O. A. Hurricane, *Phys. Plasmas* **27**(11), 112704 (2020).
- ⁴⁸V. A. Smalyuk, C. R. Weber, H. F. Robey, D. T. Casey, K.-C. Chen, D. S. Clark, M. Farrell, S. Felker, J. E. Field, S. W. Haan, B. A. Hammel, A. V. Hamza, D. Hoover, J. J. Kroll, O. L. Landen, A. G. MacPhee, D. Martinez, A. Nikroo, and N. Rice, *Phys. Plasmas* **24**, 042706 (2017).
- ⁴⁹O. A. Hurricane, D. A. Callahan, D. T. Casey, E. L. Dewald, T. R. Dittrich, T. Döppner, M. A. Barrios Garcia, D. E. Hinkel, L. F. Berzak Hopkins, P. Kervin, J. L. Kline, S. L. Pape, T. Ma, A. G. MacPhee, J. L. Milovich, J. Moody, A. E. Pak, P. K. Patel, H. S. Park, B. A. Remington, H. F. Robey, J. D. Salmonson, P. T. Springer, R. Tommasini, L. R. Benedetti, J. A. Caggiano, P. Celliers, C. Cerjan, R. Dylla-Spears, D. Edgell, M. J. Edwards, D. Fittinghoff, G. P. Grim, N. Guler, N. Izumi, J. A. Frenje, M. Galu Johnson, S. Haan, R. Hatarik, H. Herrmann, S. Khan, J. Knauer, B. J. Kozioziemski, A. L. Kritcher, G. Kyrala, S. A. MacLaren, F. E. Merrill, P. Michel, J. Ralph, J. S. Ross, J. R. Rygg, M. B. Schneider, B. K. Spears, K. Widmann, and C. B. Yeaman, *Phys. Plasmas* **21**(5), 056314 (2014).

- ⁵⁰H. S. Park, O. A. Hurricane, D. A. Callahan, D. T. Casey, E. L. Dewald, T. R. Dittrich, T. Döppner, D. E. Hinkel, L. F. Berzak Hopkins, S. Le Pape, T. Ma, P. K. Patel, B. A. Remington, H. F. Robey, J. D. Salmonson, and J. L. Kline, *Phys. Rev. Lett.* **112**, 055001 (2014).
- ⁵¹T. R. Dittrich, O. A. Hurricane, D. A. Callahan, E. L. Dewald, T. Döppner, D. E. Hinkel, L. F. Berzak Hopkins, S. Le Pape, T. Ma, J. L. Milovich, J. C. Moreno, P. K. Patel, H. S. Park, B. A. Remington, J. D. Salmonson, and J. L. Kline, *Phys. Rev. Lett.* **112**, 055002 (2014).
- ⁵²D. E. Hinkel, T. Döppner, L. P. Masse, K. Widmann, L. Divol, B. Bachmann, L. F. Berzak Hopkins, S. LePape, C. R. Weber, S. A. MacLaren, A. B. Zylstra, J. E. Ralph, L. R. Benedetti, A. S. Moore, C. A. Thomas, D. T. Casey, V. A. Smalyuk, H. F. Robey, P. M. Celliers, M. J. MacDonald, C. M. Krauland, D. B. Thorn, M. D. Rosen, P. K. Patel, B. J. MacGowan, M. B. Schneider, D. S. Clark, A. E. Pak, M. J. Edwards, O. L. Landen, D. A. Callahan, and O. A. Hurricane, *High Energy Density Phys.* **37**, 100884 (2020).
- ⁵³K. L. Baker, H. F. Robey, J. L. Milovich, O. S. Jones, V. A. Smalyuk, D. T. Casey, A. G. MacPhee, A. Pak, P. M. Celliers, D. S. Clark, O. L. Landen, J. L. Peterson, L. F. Berzak-Hopkins, C. R. Weber, S. W. Haan, T. D. Döppner, S. Dixit, E. Giraldez, A. V. Hamza, K. S. Jancaitis, J. J. Kroll, K. N. Lafontaine, B. J. MacGowan, J. D. Moody, A. Nikroo, and C. C. Widmayer, *Phys. Plasmas* **22**(5), 052702 (2015).
- ⁵⁴D. T. Casey, J. L. Milovich, V. A. Smalyuk, D. S. Clark, H. F. Robey, A. Pak, A. G. MacPhee, K. L. Baker, C. R. Weber, T. Ma, H. S. Park, T. Döppner, D. A. Callahan, S. W. Haan, P. K. Patel, J. L. Peterson, D. Hoover, A. Nikroo, C. B. Yeamans, F. E. Merrill, P. L. Volegov, D. N. Fittinghoff, G. P. Grim, M. J. Edwards, O. L. Landen, K. N. Lafontaine, B. J. MacGowan, C. C. Widmayer, D. B. Sayre, R. Hatarik, E. J. Bond, S. R. Nagel, L. R. Benedetti, N. Izumi, S. Khan, B. Bachmann, B. K. Spears, C. J. Cerjan, M. Gatu Johnson, and J. A. Frenje, *Phys. Rev. Lett.* **115**(10), 105001 (2015).
- ⁵⁵V. A. Smalyuk, H. F. Robey, T. Döppner, D. T. Casey, D. S. Clark, O. S. Jones, J. L. Milovich, J. L. Peterson, B. Bachmann, K. L. Baker, L. R. Benedetti, L. F. Berzak Hopkins, R. Bionta, E. Bond, D. K. Bradley, D. A. Callahan, P. M. Celliers, C. Cerjan, K.-C. Chen, C. Goyon, G. Grim, S. N. Dixit, M. J. Eckart, M. J. Edwards, M. Farrell, D. N. Fittinghoff, J. A. Frenje, M. Gatu-Johnson, N. Gharibyan, S. W. Haan, A. V. Hamza, E. Hartouni, R. Hatarik, M. Havre, M. Hohenberger, D. Hoover, O. A. Hurricane, N. Izumi, K. S. Jancaitis, S. F. Khan, J. P. Knauer, J. J. Kroll, G. Kyrala, K. N. LaFortune, O. L. Landen, T. Ma, B. J. MacGowan, A. G. MacPhee, M. Mauldin, F. E. Merrill, A. S. Moore, S. Nagel, A. Nikroo, A. Pak, P. K. Patel, J. E. Ralph, D. B. Sayre, D. Shaughnessy, B. K. Spears, R. Tommasini, D. P. Turnbull, A. L. Velikovich, P. L. Volegov, C. R. Weber, C. C. Widmayer, and C. Yeamans, *Phys. Plasmas* **23**, 102703 (2016).
- ⁵⁶H. F. Robey, L. Berzak Hopkins, J. L. Milovich, and N. B. Meezan, *Phys. Plasmas* **25**(1), 012711 (2018).
- ⁵⁷A. B. Zylstra, A. L. Kritch, O. A. Hurricane, D. A. Callahan, J. E. Ralph, D. T. Casey, A. Pak, O. L. Landen, B. Bachmann, K. L. Baker, L. Berzak Hopkins, S. D. Bhandarkar, J. Biener, R. M. Bionta, N. W. Birge, T. Braun, T. M. Briggs, P. M. Celliers, H. Chen, C. Choate, D. S. Clark, L. Divol, T. Döppner, D. Fittinghoff, M. J. Edwards, M. Gatu Johnson, N. Gharibyan, S. Haan, K. D. Hahn, E. Hartouni, D. E. Hinkel, D. D. Ho, M. Hohenberger, J. P. Holder, H. Huang, N. Izumi, J. Jeet, O. Jones, S. M. Kerr, S. F. Khan, H. Geppert Kleinrath, V. Geppert Kleinrath, C. Kong, K. M. Lamb, S. Le Pape, N. C. Lemos, J. D. Lindl, B. J. MacGowan, A. J. Mackinnon, A. G. MacPhee, E. V. Marley, K. Meaney, M. Millot, A. S. Moore, K. Newman, J. M. G. Di Nicola, A. Nikroo, R. Nora, P. K. Patel, N. G. Rice, M. S. Rubery, J. Sater, D. J. Schlossberg, S. M. Sepke, K. Sequoia, S. J. Shin, M. Stadermann, S. Stoupin, D. J. Strozzi, C. A. Thomas, R. Tommasini, C. Trosseille, E. R. Tubman, P. L. Volegov, C. Wild, D. T. Woods, and S. T. Yang, *Phys. Rev. E* **106**(2), 025202 (2022).
- ⁵⁸A. L. Kritch, A. B. Zylstra, D. A. Callahan, O. A. Hurricane, C. R. Weber, D. S. Clark, C. V. Young, J. E. Ralph, D. T. Casey, A. Pak, O. L. Landen, B. Bachmann, K. L. Baker, L. Berzak Hopkins, S. D. Bhandarkar, J. Biener, R. M. Bionta, N. W. Birge, T. Braun, T. M. Briggs, P. M. Celliers, H. Chen, C. Choate, L. Divol, T. Döppner, D. Fittinghoff, M. J. Edwards, M. Gatu Johnson, N. Gharibyan, S. Haan, K. D. Hahn, E. Hartouni, D. E. Hinkel, D. D. Ho, M. Hohenberger, J. P. Holder, H. Huang, N. Izumi, J. Jeet, O. Jones, S. M. Kerr, S. F. Khan, H. Geppert Kleinrath, V. Geppert Kleinrath, C. Kong, K. M. Lamb, S. Le Pape, N. C. Lemos, J. D. Lindl, B. J. MacGowan, A. J. Mackinnon, A. G. MacPhee, E. V. Marley, K. Meaney, M. Millot, A. S. Moore, K. Newman, J. M. G. Di Nicola, A. Nikroo, R. Nora, P. K. Patel, N. G. Rice, M. S. Rubery, J. Sater, D. J. Schlossberg, S. M. Sepke, K. Sequoia, S. J. Shin, M. Stadermann, S. Stoupin, D. J. Strozzi, C. A. Thomas, R. Tommasini, C. Trosseille, E. R. Tubman, P. L. Volegov, C. Wild, D. T. Woods, and S. T. Yang, *Phys. Rev. E* **106**(2), 025201 (2022).

M. S. Freeman, J. Frenje, D. Frey, G. Frieders, S. Friedrich, D. H. Froula, J. Fry, T. Fuller, J. Gaffney, S. Gales, B. L. Galloudec, K. K. L. Galloudec, A. Gambhir, L. Gao, W. J. Garbett, A. Garcia, C. Gates, E. Gaut, P. Gauthier, Z. Gavin, J. Gaylord, M. Geissel, F. Genin, J. Georges, H. Geppert-Kleinrath, V. Geppert-Kleinrath, N. Gharibyan, J. Gibson, C. Gibson, E. Giraldez, V. Glebov, S. G. Glendinning, S. Glenn, S. H. Glenzer, S. Goade, P. L. Gobby, S. R. Goldman, B. Golick, M. Gomez, V. Goncharov, D. Goodin, P. Grabowski, E. Grafil, P. Graham, J. Grandy, E. Grasz, F. Graziani, G. Greenman, J. A. Greenough, A. Greenwood, G. Gregori, T. Green, J. R. Griego, G. P. Grim, J. Grondalski, S. Gross, J. Guckian, N. Guler, B. Gunney, G. Guss, S. Haan, J. Hackbarth, L. Hackel, R. Hackel, C. Haefner, C. Hagmann, K. D. Hahn, S. Hahn, B. J. Haid, B. M. Haines, B. M. Hall, C. Hall, G. N. Hall, M. Hamamoto, S. Hamel, C. E. Hamilton, B. A. Hammel, J. H. Hammer, G. Hampton, A. Hamza, A. Handler, S. Hansen, D. Hanson, R. Haque, D. Harding, E. Harding, J. D. Hares, D. B. Harris, J. A. Harte, E. P. Hartouni, R. Hatarik, S. Hatchett, A. A. Hauer, M. Havre, R. Hawley, J. Hayes, J. Hayes, S. Hayes, A. Hayes-Sterbenz, C. A. Haynam, D. A. Haynes, D. Headley, A. Heal, J. E. Heebner, S. Heerey, G. M. Heestand, R. Heeter, N. Hein, C. Heinbockel, C. Hendricks, M. Henesian, J. Heninger, J. Henrikson, E. A. Henry, E. B. Herbold, M. R. Hermann, G. Hermes, J. E. Hernandez, V. J. Hernandez, M. C. Herrmann, H. W. Herrmann, O. D. Herrera, D. Hewett, R. Hibbard, D. G. Hicks, D. Hill, K. Hill, T. Hilsabeck, D. E. Hinkel, D. D. Ho, V. K. Ho, J. K. Hoffer, N. M. Hoffman, M. Hohenberger, M. Hohensee, W. Hoke, D. Holdener, F. Holdener, J. P. Holder, B. Holko, D. Holunga, J. F. Holzrichter, J. Honig, D. Hoover, D. Hopkins, L. Berzak Hopkins, M. Hoppe, M. L. Hoppe, J. Horner, R. Hornung, C. J. Horsfield, J. Horvath, D. Hotaling, R. House, L. Howell, W. W. Hsing, S. X. Hu, H. Huang, J. Huckins, H. Hui, K. D. Humbird, J. Hund, J. Hunt, O. A. Hurricane, M. Hutton, K. H. Huynh, L. Inandan, C. Iglesias, I. V. Igumenshchev, N. Izumi, M. Jackson, J. Jackson, S. D. Jacobs, G. James, K. Jancaitis, J. Jarboe, L. C. Jarrott, D. Jasion, J. Jaquez, J. Jeet, A. E. Jenei, J. Jensen, J. Jimenez, R. Jimenez, D. Jobe, Z. Johal, H. M. Johns, D. Johnson, M. A. Johnson, M. Gatu Johnson, R. J. Johnson, S. Johnson, S. A. Johnson, T. Johnson, K. Jones, O. Jones, M. Jones, R. Jorge, H. J. Jorgenson, M. Julian, B. I. Jun, R. Jungquist, J. Kaae, N. Kabadi, D. Kaczala, D. Kalantar, K. Kangas, V. V. Karasiev, M. Karasik, V. Karpenko, A. Kasarky, K. Kasper, R. Kauffman, M. I. Kaufman, C. Keane, L. Keaty, L. Kegelmeyer, P. A. Keiter, P. A. Kellett, J. Kellogg, J. H. Kelly, S. Kemic, A. J. Kemp, G. E. Kemp, G. D. Kerbel, D. Kershaw, S. M. Kerr, T. J. Kessler, M. H. Key, S. F. Khan, H. Khater, C. Kiikka, J. Kilkenny, Y. Kim, Y. J. Kim, J. Kimko, M. Kimmel, J. M. Kindel, J. King, R. K. Kirkwood, L. Klaus, D. Klem, J. L. Kline, J. Klingmann, G. Kluth, P. Knapp, J. Knauer, J. Knipping, M. Knudson, D. Kobs, J. Koch, T. Kohut, C. Kong, J. M. Koning, P. Koning, S. Konior, H. Kornblum, B. L. Kot, B. Koziociemski, M. Kozlowski, P. M. Kozlowski, J. Krammen, N. S. Krasheninnikova, B. Kraus, W. Krauser, J. D. Kress, A. L. Kritch, E. Krieger, J. J. Kroll, W. L. Kruer, M. K. G. Kruse, S. Kucheyev, M. Kumbera, S. Kumpan, J. Kunimune, B. Kustowski, T. J. T. Kwan, G. A. Kyrala, S. Laffite, M. Lafon, K. LaFortune, B. Lahmann, B. Lairson, O. L. Landen, J. Langenbrunner, L. Lagin, T. Land, M. Lane, D. Laney, A. B. Langdon, S. H. Langer, A. Langro, N. E. Lanier, T. E. Lanier, D. Larson, B. F. Lasinski, D. Lassle, D. LaTray, G. Lau, N. Lau, C. Laumann, A. Laurence, T. A. Laurence, J. Lawson, H. P. Le, R. R. Leach, L. Leal, A. Leatherland, K. LeChien, B. Lechleiter, A. Lee, M. Lee, T. Lee, R. J. Leeper, E. Lefebvre, J. P. Leidinger, B. LeMire, R. W. Lemke, N. C. Lemos, S. Le Pape, R. Lerche, S. Lerner, S. Letts, K. Levedahl, T. Lewis, C. K. Li, H. Li, J. Li, W. Liao, Z. M. Liao, D. Liedahl, J. Lieberman, G. Lindford, E. L. Lindman, J. D. Lindl, H. Loey, R. A. London, F. Long, E. N. Loomis, F. E. Lopez, H. Lopez, E. Losbanos, S. Loucks, R. Lowe-Webb, E. Lundgren, A. P. Ludwigsen, R. Luo, J. Lusk, R. Lyons, T. Ma, Y. Macallop, M. J. MacDonald, B. J. MacGowan, J. M. Mack, A. J. Mackinnon, S. A. McLaren, A. G. MacPhee, G. R. Magelssen, J. Magoon, R. M. Malone, T. Malsbury, R. Managan, R. Mancini, K. Manes, D. Maney, D. Manha, O. M. Mannion, A. M. Manuel, E. Mapoles, G. Mara, T. Marcotte, E. Marin, M. M. Marinak, C. Mariscal, D. A. Mariscal, E. F. Mariscal, E. V. Marley, J. A. Marozas, R. Marquez, C. D. Marshall, F. J. Marshall, M. Marshall, S. Marshall, J. Marticorena, D. Martinez, I. Maslennikov, D. Mason, R. J. Mason, L. Masse, W. Massey, P. E. Masson-Labordre, N. D. Masters, D. Mathisen, E. Mathison, J. Matone, M. J. Matthews, C. Mattoon, T. R. Mattsson, K. Matzen, C. W. Mauche, M. Mauldin, T. McAbee, M. McBurney, T. McCarville, R. L. McCrory, A. M. McEvoy, C. McGuffey, M. McInnis, P.

McKenty, M. S. McKinley, J. B. McLeod, A. McPherson, B. McQuillan, M. Meamber, K. D. Meaney, N. B. Meezan, R. Meissner, T. A. Mehlhorn, N. C. Mehta, J. Menapace, F. E. Merrill, B. T. Merritt, E. C. Merritt, D. D. Meyerhofer, S. Mezyk, R. J. Mich, P. A. Michel, D. Milam, C. Miller, D. Miller, D. S. Miller, E. Miller, E. K. Miller, J. Miller, M. Miller, P. E. Miller, T. Miller, W. Miller, V. Miller-Kamm, M. Millot, J. L. Milovich, P. Minner, J. L. Miquel, S. Mitchell, K. Molvig, R. C. Montesanti, D. S. Montgomery, M. Monticelli, A. Montoya, J. D. Moody, A. S. Moore, E. Moore, M. Moran, J. C. Moreno, K. Moreno, B. E. Morgan, T. Morrow, J. W. Morton, E. Moses, K. Moy, R. Muir, M. S. Murillo, J. E. Murray, J. R. Murray, D. H. Munro, T. J. Murphy, F. M. Munteanu, J. Nafziger, T. Nagayama, S. R. Nagel, R. Nast, R. A. Negres, A. Nelson, D. Nelson, J. Nelson, S. Nelson, S. Nemethy, P. Neumayer, K. Newman, M. Newton, H. Nguyen, J. G. Di Nicola, P. Di Nicola, C. Niemann, A. Nikroo, P. M. Nilson, A. Nobile, V. Noorai, R. Nora, M. Norton, M. Nostrand, V. Note, S. Novell, P. F. Nowak, A. Nunez, R. A. Nyholm, M. O'Brien, A. Ocegueda, J. A. Oertel, J. Okui, B. Olejniczak, J. Oliveira, P. Olsen, B. Olson, K. Olson, R. E. Olson, Y. P. Opachich, N. Orsi, C. D. Orth, M. Owen, S. Padalino, E. Padilla, R. Paguio, S. Paguio, J. Paisner, S. Pajoom, A. Pak, S. Palaniyappan, K. Palma, T. Pannell, F. Papp, D. Paras, T. Parham, H. S. Park, A. Pasternak, S. Patankar, M. V. Patel, P. K. Patel, R. Patterson, S. Patterson, B. Paul, M. Paul, E. Pauli, O. T. Pearce, J. Pearcey, B. Pedrotti, A. Peer, L. J. Pelz, B. Penetrante, J. Penner, A. Perez, L. J. Perkins, E. Pernice, T. S. Perry, S. Person, D. Petersen, T. Petersen, D. L. Peterson, E. B. Peterson, J. E. Peterson, J. L. Peterson, K. Peterson, R. R. Peterson, R. D. Petrasso, F. Philippe, T. J. Phipps, E. Piceno, Y. Ping, L. Pickworth, J. Pino, R. Plummer, G. D. Pollack, S. M. Pollaine, B. B. Pollock, D. Ponce, J. Ponce, J. Pontelandolfo, J. L. Porter, J. Post, O. Poujade, C. Powell, H. Powell, G. Power, M. Pozulp, M. Prantil, M. Prasad, S. Pratuch, S. Price, K. Primdahl, S. Prisbrey, R. Procassini, A. Pruyne, B. Pudliner, S. R. Qiu, K. Quan, M. Quinn, J. Quintenz, P. B. Radha, F. Rainer, J. E. Ralph, K. S. Raman, R. Raman, P. Rambo, S. Rana, A. Randewich, D. Rardin, M. Ratledge, N. Ravelo, F. Ravizza, M. Rayce, A. Raymond, B. Raymond, B. Reed, C. Reed, S. Regan, B. Reichelt, V. Reis, S. Reisdorf, V. Rekow, B. A. Remington, A. Rendon, W. Requieron, M. Rever, H. Reynolds, J. Reynolds, J. Rhodes, M. Rhodes, M. C. Richardson, B. Rice, N. G. Rice, R. Rieben, A. Rigatti, S. Riggs, H. G. Rinderknecht, K. Ring, B. Riordan, R. Riquer, C. Rivers, D. Roberts, V. Roberts, G. Robertson, H. F. Robey, J. Robles, P. Rocha, G. Rochau, J. Rodriguez, S. Rodriguez, M. Rosen, M. Rosenberg, G. Ross, J. S. Ross, P. Ross, J. Rouse, D. Rovang, A. M. Rubenchik, M. S. Rubery, C. L. Ruiz, M. Rushford, B. Russ, J. R. Rygg, B. S. Ryujin, R. A. Sacks, R. F. Sacks, K. Saito, T. Salmon, J. D. Salmonson, J. Sanchez, S. Samuelson, M. Sanchez, C. Sangster, A. Saroyan, J. Sater, A. Satsangi, S. Sauras, R. Saunders, J. P. Sauppe, R. Sawicki, D. Sayre, M. Scanlan, K. Schaffers, G. T. Schappert, S. Schiaffino, D. J. Schlossberg, D. W. Schmidt, M. J. Schmitt, D. H. G. Schneider, M. B. Schneider, R. Schneider, M. Schöff, M. Schollmeier, M. Scholmerich, C. R. Schroeder, S. E. Schrauth, H. A. Scott, I. Scott, J. M. Scott, R. H. H. Scott, C. R. Scullard, T. Sedillo, F. H. Seguin, W. Seka, J. Senecal, S. M. Sepke, L. Seppala, K. Sequoia, J. Severyn, J. M. Sevier, N. Sewell, S. Seznec, R. C. Shah, J. Shamlian, D. Shaughnessy, M. Shaw, R. Shaw, C. Shearer, R. Shelton, N. Shen, M. W. Sherlock, A. I. Shestakov, E. L. Shi, S. J. Shin, N. Shingleton, W. Shmaya, M. Shor, M. Shoup, C. Shuldberg, L. Siegel, F. J. Silva, A. N. Simakov, B. T. Sims, D. Sinars, P. Singh, H. Sio, K. Skulina, S. Skupsky, S. Slutz, M. Sluyter, V. A. Smalyuk, D. Smauley, R. M. Smeltser, C. Smith, I. Smith, J. Smith, L. Smith, R. Smith, R. Sohn, S. Sommer, C. Sorce, M. Sorem, J. M. Soures, M. L. Spaeth, B. K. Spears, S. Spears, D. Speck, R. Speck, J. Spears, T. Spinka, P. T. Springer, M. Stadermann, B. Stahl, J. Stahoviak, L. G. Stanton, R. Steele, W. Steele, D. Steinman, R. Stemke, R. Stephens, S. Sterbenz, P. Sterne, D. Stevens, J. Stevens, C. B. Still, C. Stoeckl, W. Stoeffl, J. S. Stolken, C. Stoltz, E. Storm, G. Stone, S. Stoupin, E. Stout, I. Stowers, R. Strauser, H. Strecker, J. Streit, D. J. Strozzi, T. Suratwala, G. Sutcliffe, L. J. Suter, S. B. Sutton, V. Svidzinski, G. Swadling, W. Sweet, A. Szoke, M. Tabak, M. Takagi, A. Tambazidis, V. Tang, M. Taranowski, L. A. Taylor, S. Telford, W. Theobald, M. Thi, A. Thomas, C. A. Thomas, I. Thomas, R. Thomas, I. J. Thompson, A. Thongtisubkul, C. B. Thorsness, G. Tietbohl, R. E. Tipton, M. Tobin, N. Tomlin, R. Tommasini, A. J. Toreja, J. Torres, R. P. J. Town, S. Townsend, J. Trenholme, A. Trivelpiece, C. Trosseille, H. Truax, D. Trummer, S. Trummer, T. Truong, D. Tubbs, E. R. Tubman, T. Tunnell, D. Turnbull, R. E. Turner, M. Ulitsky, R. Upadhye, J. L. Vaher, P. VanArsdall, D. VanBlarcom,

- M. Vandenboomgaerde, R. VanQuinlan, B. M. Van Wonterghem, W. S. Varnum, A. L. Velikovich, A. Vella, C. P. Verdon, B. Vermillion, S. Vernon, R. Vesey, J. Vickers, R. M. Vignes, M. Visosky, J. Vocke, P. L. Volegov, S. Vonhof, R. Von Rotz, H. X. Vu, M. Vu, D. Wall, J. Wall, R. Wallace, B. Wallin, D. Walmer, C. A. Walsh, C. F. Walters, C. Waltz, A. Wan, A. Wang, Y. Wang, J. S. Wark, B. E. Warner, J. Watson, R. G. Watt, P. Watts, J. Weaver, R. P. Weaver, S. Weaver, C. R. Weber, P. Weber, S. V. Weber, P. Wegner, B. Welday, L. Welser-Sherrell, K. Weiss, K. Widmann, G. F. Wheeler, W. Whistler, R. K. White, H. D. Whitley, P. Whitman, M. E. Wickett, C. Widmayer, J. Wiedwald, R. Wilcox, S. Wilcox, C. Wild, B. H. Wilde, C. H. Wilde, K. Wilhelmsen, M. D. Wilke, H. Wilkens, P. Wilkins, S. C. Wilks, E. A. Williams, G. J. Williams, W. Williams, W. H. Williams, D. C. Wilson, B. Wilson, E. Wilson, R. Wilson, S. Winters, J. Wisoff, M. Wittman, J. Wolfe, A. Wong, K. W. Wong, L. Wong, N. Wong, R. Wood, D. Woodhouse, J. Woodruff, D. T. Woods, S. Woods, B. N. Woodworth, E. Wooten, A. Wootton, K. Work, J. B. Workman, J. Wright, M. Wu, C. Wuest, F. J. Wysocki, H. Xu, M. Yamaguchi, B. Yang, S. T. Yang, J. Yatabe, C. B. Yeamans, B. C. Yee, S. A. Yi, L. Yin, B. Young, C. S. Young, C. V. Young, P. Young, K. Youngblood, R. Zacharias, G. Zagaris, N. Zaitseva, F. Zaka, F. Ze, B. Zeiger, M. Zika, G. B. Zimmerman, T. Zobrist, J. D. Zuegel, A. B. Zylstra, and Indirect Drive ICF Collaboration, *Phys. Rev. Lett.* **129**(7), 075001 (2022).
- ⁶⁰V. N. Goncharov, T. C. Sangster, R. Betti, T. R. Boehly, M. J. Bonino, T. J. B. Collins, R. S. Craxton, J. A. Delettrez, D. H. Edgell, R. Epstein, R. K. Follett, C. J. Forrest, D. H. Froula, V. Y. Glebov, D. R. Harding, R. J. Henchen, S. X. Hu, I. V. Igumenshchev, R. Janezic, J. H. Kelly, T. J. Kessler, T. Z. Kosc, S. J. Loucks, J. A. Marozas, F. J. Marshall, A. V. Maximov, R. L. McCrory, P. W. McKenty, D. D. Meyerhofer, D. T. Michel, J. F. Myatt, R. Nora, P. B. Radha, S. P. Regan, W. Seka, W. Shmydaya, R. W. Short, A. Shvydky, S. Skupsky, C. Stoeckl, B. Yaakobi, J. A. Frenje, M. Gatou-Johnson, R. D. Petrasco, and D. T. Casey, *Phys. Plasmas* **21**, 56315 (2014).
- ⁶¹H. F. Robey, P. M. Celliers, J. L. Kline, A. J. Mackinnon, T. R. Boehly, O. L. Landen, J. H. Eggert, D. Hicks, S. Le Pape, D. R. Farley, M. W. Bowers, K. G. Krauter, D. H. Munro, O. S. Jones, J. L. Milovich, D. Clark, B. K. Spears, R. P. Town, S. W. Haan, S. Dixit, M. B. Schneider, E. L. Dewald, K. Widmann, J. D. Moody, T. D. Döppner, H. B. Radousky, A. Nikroo, J. J. Kroll, A. V. Hamza, J. B. Horner, S. D. Bhandarkar, E. Dzenitis, E. Alger, E. Giraldez, C. Castro, K. Moreno, C. Haynam, K. N. LaFortune, C. Widmayer, M. Shaw, K. Jancaitis, T. Parham, D. M. Holunga, C. F. Walters, B. Haid, T. Malsbury, D. Trummer, K. R. Coffee, B. Burr, L. V. Berzins, C. Choate, S. J. Brereton, S. Azevedo, H. Chandrasekaran, S. Glenzer, J. A. Caggiano, J. P. Knauer, J. A. Frenje, D. T. Casey, M. G. Johnson, F. H. Seguin, B. K. Young, M. J. Edwards, B. M. Van Wonterghem, J. Kilkenny, B. J. MacGowan, J. Atherton, J. D. Lindl, D. D. Meyerhofer, and E. Moses, *Phys. Rev. Lett.* **108**(21), 215004 (2012).
- ⁶²O. L. L. Landen, R. Benedetti, D. Bleuel, T. R. R. Boehly, D. K. K. Bradley, J. A. A. Caggiano, D. A. A. Callahan, P. M. M. Celliers, C. J. J. Cerjan, D. Clark, G. W. W. Collins, E. L. L. Dewald, S. N. N. Dixit, T. Doeppner, D. Edgell, J. Eggert, D. Farley, J. A. A. Frenje, V. Glebov, S. M. M. Glenn, S. H. H. Glenzer, S. W. W. Haan, A. Hamza, B. A. A. Hammel, C. A. A. Haynam, J. H. H. Hammer, R. F. F. Heeter, H. W. W. Herrmann, D. G. G. Hicks, D. E. E. Hinkel, N. Izumi, M. Gatou Johnson, O. S. S. Jones, D. H. H. Kalantar, R. L. L. Kauffman, J. D. D. Kilkenny, J. L. L. Kline, J. P. P. Knauer, J. A. A. Koch, G. A. A. Kyrala, K. Lafontaine, T. Ma, A. J. J. MacKinnon, A. J. J. MacPhee, E. Mapoles, J. L. L. Milovich, J. D. D. Moody, N. B. B. Meezan, P. Michel, A. S. S. Moore, D. H. H. Munro, A. Nikroo, R. E. E. Olson, K. Opachich, A. Pak, T. Parham, P. Patel, H.-S. Park, R. P. P. Petrasco, J. Ralph, S. P. P. Regan, B. A. A. Remington, H. G. G. Rinderknecht, H. F. F. Robey, M. D. D. Rosen, J. S. S. Ross, J. D. D. Salmonson, T. C. C. Sangster, M. B. B. Schneider, V. Smalyuk, B. K. K. Spears, P. T. T. Springer, L. J. J. Suter, C. A. A. Thomas, R. P. J. Town, S. V. V. Weber, P. J. J. Wegner, D. C. C. Wilson, K. Widmann, C. Yeaman, A. Zylstra, M. J. J. Edwards, J. D. D. Lindl, L. J. J. Atherton, W. W. W. Hsing, B. J. J. MacGowan, B. M. M. Van Wonterghem, and E. I. I. Moses, *Plasma Phys. Controlled Fusion* **54**, 124026 (2012).
- ⁶³O. A. Hurricane, *et al.*, *Phys. Plasmas* **29**, 12703 (2022).
- ⁶⁴D. T. Casey, O. L. Landen, E. Hartouni, R. M. Bionta, K. D. Hahn, P. L. Volegov, D. N. Fittinghoff, V. Geppert-Kleinrath, C. H. Wilde, J. L. Milovich, V. A. Smalyuk, J. E. Field, O. A. Hurricane, A. B. Zylstra, A. L. Kritch, D. S. Clark, C. V. Young, R. C. Nora, D. A. Callahan, B. J. MacGowan, D. H. Munro, B. K. Spears, J. L. Peterson, J. A. Gaffney, K. D. Humbird, M. K. G. Kruse, A. S. Moore, D. J. Schlossberg, M. Gatou-Johnson, and J. A. Frenje, *Phys. Plasmas* **28**(4), 042708 (2021).
- ⁶⁵O. L. Landen, D. T. Casey, J. M. DiNicola, T. Doeppner, E. P. Hartouni, D. E. Hinkel, L. F. Berzak Hopkins, M. Hohenberger, A. L. Kritch, S. LePape, B. J. MacGowan, S. Maclare, K. D. Meaney, M. Millot, P. K. Patel, J. Park, L. A. Pickworth, H. F. Robey, J. S. Ross, S. T. Yang, A. B. Zylstra, K. L. Baker, D. A. Callahan, P. M. Celliers, M. J. Edwards, O. A. Hurricane, J. D. Lindl, J. D. Moody, J. Ralph, V. A. Smalyuk, C. A. Thomas, B. M. Van Wonterghem, and C. R. Weber, *High Energy Density Phys.* **36**, 100765 (2020).
- ⁶⁶T. Döppner, D. A. Callahan, O. A. Hurricane, D. E. Hinkel, T. Ma, H. S. Park, L. F. Berzak Hopkins, D. T. Casey, P. Celliers, E. L. Dewald, T. R. Dittrich, S. W. Haan, A. L. Kritch, A. MacPhee, S. Le Pape, A. Pak, P. K. Patel, P. T. Springer, J. D. Salmonson, R. Tommasini, L. R. Benedetti, E. Bond, D. K. Bradley, J. Caggiano, J. Church, S. Dixit, D. Edgell, M. J. Edwards, D. N. Fittinghoff, J. Frenje, M. Gatou Johnson, G. Grim, R. Hatarik, M. Havre, H. Herrmann, N. Izumi, S. F. Khan, J. L. Kline, J. Knauer, G. A. Kyrala, O. L. Landen, F. E. Merrill, J. Moody, A. S. Moore, A. Nikroo, J. E. Ralph, B. A. Remington, H. F. Robey, D. Sayre, M. Schneider, H. Strecker, R. Town, D. Turnbull, P. L. Volegov, A. Wan, K. Widmann, C. H. Wilde, and C. Yeaman, *Phys. Rev. Lett.* **115**(5), 055001 (2015).
- ⁶⁷P. Amendt, D. Ho, Y. Ping, V. Smalyuk, S. Khan, J. Lindl, D. Strozzi, R. Tommasini, M. Belyaev, C. Cerjan, O. Jones, W. Krue, N. Meezan, H. Robey, F. Tsung, C. Weber, and C. Young, *Phys. Plasmas* **26**(8), 082707 (2019).
- ⁶⁸D. E. Hinkel, L. F. Berzak Hopkins, T. Ma, J. E. Ralph, F. Albert, L. R. Benedetti, P. M. Celliers, T. Döppner, C. S. Goyon, N. Izumi, L. C. Jarrott, S. F. Khan, J. L. Kline, A. L. Kritch, G. A. Kyrala, S. R. Nagel, A. E. Pak, P. Patel, M. D. Rosen, J. R. Rygg, M. B. Schneider, D. P. Turnbull, C. B. Yeaman, D. A. Callahan, and O. A. Hurricane, *Phys. Rev. Lett.* **117**(22), 225002 (2016).
- ⁶⁹A. L. Kritch, C. V. Young, H. F. Robey, C. R. Weber, A. B. Zylstra, O. A. Hurricane, D. A. Callahan, J. E. Ralph, J. S. Ross, K. L. Baker, D. T. Casey, D. S. Clark, T. Döppner, L. Divol, M. Hohenberger, L. Berzak Hopkins, S. Le Pape, N. B. Meezan, A. Pak, P. K. Patel, R. Tommasini, S. J. Ali, P. A. Amendt, L. J. Atherton, B. Bachmann, D. Bailey, L. R. Benedetti, R. Betti, S. D. Bhandarkar, J. Biener, R. M. Bionta, N. W. Birge, E. J. Bond, D. K. Bradley, T. Braun, T. M. Briggs, M. W. Bruhn, P. M. Celliers, B. Chang, T. Chapman, H. Chen, C. Choate, A. R. Christopher, J. W. Crippen, E. L. Dewald, T. R. Dittrich, M. J. Edwards, W. A. Farmer, J. E. Field, D. Fittinghoff, J. A. Frenje, J. A. Gaffney, M. Gatou Johnson, S. H. Glenser, G. P. Grim, S. Haan, K. D. Hahn, G. N. Hall, B. A. Hammel, J. Harte, E. Hartouni, J. E. Heebner, V. J. Hernandez, H. Herrmann, M. C. Herrmann, D. E. Hinkel, D. D. Ho, J. P. Holder, W. W. Hsing, H. Huang, K. D. Humbird, N. Izumi, L. C. Jarrott, J. Jeet, O. Jones, G. D. Kerbel, S. M. Kerr, S. F. Khan, J. Kilkenny, Y. Kim, H. Geppert-Kleinrath, V. Geppert-Kleinrath, C. Kong, J. M. Koning, M. K. G. Kruse, J. J. Kroll, B. Kustowski, O. L. Landen, S. Langer, D. Larson, N. C. Lemos, J. D. Lindl, T. Ma, M. J. MacDonald, B. J. MacGowan, A. J. Mackinnon, S. A. McLaren, A. G. MacPhee, M. M. Marinak, D. A. Mariscal, E. V. Marley, L. Masse, K. Meaney, P. A. Michel, M. Millot, J. L. Milovich, J. D. Moody, A. S. Moore,

J. W. Morton, T. Murphy, K. Newman, J.-M. G. Di Nicola, A. Nikroo, R. Nora, M. V. Patel, L. J. Pelz, J. L. Peterson, Y. Ping, B. B. Pollock, M. Ratledge, N. G. Rice, H. Rinderknecht, M. Rosen, M. S. Rubery, J. D. Salmonson, J. Sater, S. Schiaffino, D. J. Schlossberg, M. B. Schneider, C. R. Schroeder, H. A. Scott, S. M. Sepke, K. Sequoia, M. W. Sherlock, S. Shin, V. A. Smalyuk, B. K. Spears, P. T. Springer, M. Stadermann, S. Stoupin, D. J. Strozzi, L. J. Suter, C. A. Thomas, R. P. J. Town, C. Trosseille, E. R. Tubman, P. L. Volegov, K. Widmann, C. Wild, C. H. Wilde, B. M. Van Wonterghem,

D. T. Woods, B. N. Woodworth, M. Yamaguchi, S. T. Yang, and G. B. Zimmerman, *Nat. Phys.* **18**, 251–258 (2022).

⁷⁰K. L. Baker, “Adiabat Shaping N210808 to increase DSR and robustness to capsule defects,” LLNL proposal, 2022.

⁷¹L. Berzak Hopkins, L. Divol, C. Weber, S. Le Pape, N. B. Meezan, J. S. Ross, R. Tommasini, S. Khan, D. D. Ho, J. Biener, E. Dewald, C. Goyon, C. Kong, A. Nikroo, A. Pak, N. Rice, M. Stadermann, C. Wild, D. Callahan, and O. Hurricane, *Phys. Plasmas* **25**(8), 080706 (2018).